COMPARISON OF LIKELIHOOD OF HOTSPOT FORMATION IN ENERGETIC MATERIALS DUE TO SPHERICAL AND PLANAR IMPACT

by

Meghana Sudarshan

A Thesis

Submitted to the Faculty of Purdue University

In Partial Fulfillment of the Requirements for the degree of

Master of Science in Aeronautics and Astronautics

School of Aeronautics and Astronautics

West Lafayette, Indiana

August 2021

THE PURDUE UNIVERSITY GRADUATE SCHOOL
STATEMENT OF COMMITTEE APPROVAL

Dr. Vikas Tomar, Chair

School of Aeronautics and Astronautics

Dr. Wenbin Yu

School of Aeronautics and Astronautics

Dr. Arun Prakash

School of Civil Engineering

Approved by:

Dr. Gregory A. Blaisdell

Dedicated to my family.

ACKNOWLEDGMENTS

I would like to extend my deepest gratitude to my advisor Dr. Vikas Tomar, for the constant support, and guidance throughout this work. I would like to thank Abhijeet Dhiman for all the intuitive discussions on ways of tackling the formulated problem in the current work. I very much appreciate the efforts of Ayotomi Olokun and Chandra Prakash for the great amount of assistance with the initial setup of the framework. I would also like to show gratitude to my committee members- Dr. Wenbin Yu and Dr. Arun Prakash for their efforts and contributions to this work.

Finally, I would like to thank my friends and family for being there through all the ups and downs and offering encouragement when I needed the most.

Meghana Sudarshan

TABLE OF CONTENTS

LIST OF TABLES

LIST OF FIGURES

LIST OF ABBREVIATIONS

SI	Spherical Impact
PI	Planar Impact
EM	Energetic Materials
CFEM	Cohesive Finite Element Method
HTPB	Hydroxy-Terminated Polybutadiene Binder

ABSTRACT

Energetic materials are widely used as rocket propellants and explosives in the field of aerospace and defense. Understanding the nature of impact in polymer-bonded explosives is crucial safety and transportation of energetic materials. The formation of hotpots in energetic materials leads to unexpected initiations, posing a safety hazard. An attempt was made to study the mechanical behavior of energetic materials under different shapes of impactors. In particular, the likelihood of hotspot formations was discussed in spherical and Spherical Impactors (SI). Spherical and planar-shaped impactors were modeled with a cohesive finite element framework to simulate the behavior of granular energetic materials with cyclo-tetramethylene-tetranitramine(HMX) embedded in a hydroxyl-polybutadiene binder. Temperature distribution and stresses induced around crystals on expanding stress profile of SI and uniform pressure profile from a SI are compared to determine the possibility of detonation.

In this work, the dependence of sample morphology on induced stresses in the microstructure is highlighted by using three different microstructures. A digitized polymer-bonded-explosive microstructure was analyzed for possible initiations with different impact velocities. The effect of the shape of grains and volume fractions on the likeliness of hotspot formation were studied using rounded and sharp-edged idealized crystals. Impactor behavior on samples was compared based on force chains, temperature profiles, and stress distributions.

1. INTRODUCTION

Energetic materials (EMs) consist of oxidizer crystals and polymer binder, react to external stimulations to release large amounts of chemical energy. Some oxidizers include Cyclotertramethylene tetranitramine(HMX), cyclotetramethylene trinitramine (RDX), ammonium dinitramine. Some binders include Hydroxy-terminated polybutadiene (HTPB), hydroxy-terminated polyethylene (HTPE), and polycaprolactone glycol (PEG). Many EM can be considered as propellants, explosives, or pyrotechnics as gunpowder. Understanding the causes and mechanisms of initiations in such materials is of prime importance in preventing unintended initiations during storage and transportation. Hotspots are regions in the microstructure where chemical reactions causing detonations initiate.

Nature of impact may differ based on the size and shape of the impactor. Impactors considerable to the size of sample leads to formation of expanding spherical stress waves in the structure. Impactors with a very high size ratio with sample act as a SI, create uniform waves in the microstructure. In this work, a computational study was performed with spherical and SIs to determine the likelihood of failure or detonation of EM under impact. Stress and temperature distribution profiles were used to predict hotpot formations in HTPB-HMX microstructure. Chemical behavior of energetic materials under impact is not dealt with in this study. A digitized polymer-bonded-explosive (PBX) and idealized microstructures with circular and rectangular crystals with varying volume fractions were used to study the mechanism for impact induced failure.

This thesis is divided into four chapters. Chapter 1 provides an outline pointing out key objectives of the study. Chapter 2 delivers a manuscript of the completed work. This chapter is subdivided into four sub-chapters. Section 2.1 presents a comprehensive view of the problem statement with literature review on impact-induced failure analysis of energetic materials. Section 2.2 describes the numerical methods used in this work. It explains the cohesive finite element method framework used, with Viscoplastic model and cohesive law used to model bulk elements and cohesive elements of polymer bonded explosive samples. It also illustrates modeling of planar and SIs. Section 2.3 discusses the results obtained from this study. The model is first validated with experimental results of impact on HMX-HTPB samples. Results of simulation are presented as two categories. Effects of velocity and force chains on likelihood of hotspot formation is highlighted in digitized PBX microstructures. Effects of size, shape, and volume fractions with emphasis on crystal

morphology is highlighted in idealized microstructures with circular and rectangular shaped crystals. Chapter 3 provides a summary of the key findings in this study with future work on Chapter 4.

2. COMPARISON OF LIKELIHOOD OF HOTSPOT FORMATION IN ENERGETIC MATERIALS DUE TO SPHERICAL AND PLANAR IMPACT

Meghana Sudarshan[1], Ayotomi Olokun[1], Abhijeet Dhiman[1], Vikas Tomar[1]*
[1]School of Aeronautics and Astronautics, Purdue University, USA
*Corresponding author, Phone: (765)-494-3006 Fax: (765) 494-0307 Email: tomar@purdue.edu
Manuscript Under Preparation.

ABSTRACT

Energetic materials are used as solid rocket propellants in the aerospace industry and explosives in civil and defense industry. For safe transportation and storage of energetic materials, having a good understanding of mechanical and chemical behavior of materials helps prevent unintended initiations from mechanical stimulants. In this work, the behavior of energetic material to different types of mechanical stimulant is discussed. The current understanding of deflagration modes and initiation lacks detailed information on hotspot formation mechanisms due to different nature of the impact or shape of impactor. Studies on deflagration to detonation transition focus mainly on planar impact scenarios with detonation under shock. In this study, we compare the likeliness of hotspot formation with different geometries of the impactor. A cohesive finite element (CFEM) based computational framework is used to simulate the behavior of granular energetic materials with cyclotetramethylene-tetranitramine (HMX) embedded in hydroxyl-terminated polybutadiene binder (HTPB) with planar and SI profiles. Comparison of the likelihood of detonation is highlighted based on stresses induced around the crystals in energetic on expanding stress profile of SI and uniform pressure profile from a SI.

Keywords: Energetic Material, CFEM, Spherical impact

2.1 Introduction

Energetic materials (EMs) release chemical energy stored in their structure with external stimulation like heat, impact and shock. These materials consist of explosive oxidizer crystals, constituting 60-90% by mass embedded in polymer binders. Energetic materials are found in various propellants, explosives, fuels, and pyrotechnics in aerospace and defense applications [1]. HMX is one such example of crystalline oxidizer embedded in hydroxyl-terminated polybutadiene (HTPB), which acts as a polymeric binder. Mechanical properties of binders form an essential component of polymer-bonded explosives as they absorb mechanical loads before being transferred to the crystals[2]. With external stimulations like impact, vibrations or an abrupt change in temperature, initiation and detonation of such materials can occur unintentionally [3]. Stresses may develop in the order of several GPa in short durations after impact, creating a need to quantify the conditions to understand mechanisms leading to such initiation [1].

Defects in the microstructure of these polymer-bonded explosives (PBXs) can be the regions, called hotspots, where chemical reactions causing detonation might start depending on their size, temperature, and duration of hotspots necessary [4]. Primary causes of failure due to hotspots have been linked to fracture in crystal, interfacial failure between binder and crystal, and cavitation and pore-collapse [5]. Interfacial failure between the crystal and the binder [6] is studied with various compositions observed the failure to initiate around large crystals perpendicular to the loading direction. Interface chemistry and other mechanical properties affecting the failure of energetic particles have been studied by Prakash et al. [7], [8]. Various studies have addressed the role of the microstructure and crystal morphology in energetic materials, causing failure in the structure. Effects of particle size [9] have been studied experimentally with strain rates of around 10^3 s^{-1} [4].

Hot spot mechanisms in energetic materials suggested for ignition include adiabatic compression of trapped gas spaces, mechanisms involving cavity collapse including viscous or plastic heating of the surrounding matrix material, viscous heating of material due to impacting surfaces, a mechanical failure caused by localized adiabatic shear, and increase in temperature at crack tips [[1]. Ignition sensitivity of PBX is examined based on local temperature rise, size of the hotspot, and spatial distribution, which may lead to reaction initiation if reached a critical level [[10][2]. This study uses initiation of the energetic materials due to localized adiabatic shear to describe hotspots formation, which might lead to the initiation of an explosion.

Using computational methods to understand the microstructure, chemistry, and mechanisms of failure in EMs provides a convenient and safer way in comparison to experimental methods. Linear elastic fracture mechanics method is hardly used due to crack tip singularity in large plastic deformations when the crack grows. The extended finite element method relies on initial crack location. In comparison, Cohesive zone models use cohesive elements described as cohesive forces used to pull the bulk materials apart to simulate crack initiation or growth. Significant amount of research has been carried out in the past few decades on modeling cohesive surfaces and cracks under shock compression. Cohesive finite element framework was used to analyze dynamic fracture considering plasticity at crack tip [3].

Safety of such materials during storage and transportation is of primary concern due to various impact scenarios causing unintended initiations. Impact velocities range from less than a few meters per second (could lead to deflagration) to a few kilometers per second (lead to shock detonation) of EM. Many researchers discuss the transition from detonation to deflagration modes in explosives with varying degrees of impact [11]. As discussed above, factors like grain size, material composition, impact velocity, and geometry of the material affect the modes of deflagration. The hotspots leading to the initiation of chemical reactions occur locally within the microstructure in the initial stages of failure of the material. Hotspots formed depend on various degrees of porosity of the microstructure leading to deflagration, were studied by Parker et al.[12] .The effect of impact velocity on the formation of hotspots leading to initiation was studied by Yang et al. [13] numerically. Though ignition mechanisms in low impact velocity are complex, computation and numerical studies can be used to design better materials for the safety of energetic materials during transportation.

Computational methods used in the literature take into account an impact with a planar wave on to the sample. However, in particle scenarios, the impact conditions are not limited to planar conditions. The sensitivity of energetic material to spherical-shaped objects producing spherical waves from the impact has not been studied before. The nature of impact-induced waves can determine the concentration of hotspots in the microstructure causing deflagration or detonation in the material [11].

In this work, computational models of impact samples based on CFEM were set up to effectively mimic different profiles of impactors in energetic materials. The effect of the shape of the impactor (spherical and SIs), was analyzed based on the likeliness of hotspot formation. The focus of the study

was to observe possible initiations due to the nature of the impact in the initial time steps of impact in different impactors. Initially, a digitized PBX microstructure[14] was used to observe the difference in force chains, temperature profile, and stress wave propagation in both impacts. The effects of crystal shapes and volume fraction on hotspot formation are studied in the next section with planar and SIs. Rounded and sharp-edged crystals were considered with volume fractions varying from 40-80% based on previous work [15].

2.2 Numerical Methods

2.2.1 Cohesive Finite Element Method Framework

Cohesive finite element framework (CFEM) is used for failure analysis under planar impact in previous studies[2], [14]–[19]. Effects of interface chemistry and strain rate were studied by Prakash et al [8], [17] for HTPB-AP (Ammonium Perchlorate) material properties. A similar analysis was done on HTPB-HMX by studying hotspot densities in various idealized microstructures [15] as used in this study. Other composite materials, polymers, metals were also analyzed using CFEM [20] to understand the behavior of fracture and impact failure.

In this work, a two-dimensional CFEM model was used to analyze spherical and planar impact in microstructures with cohesive surfaces defined along all the bulk element boundaries to predict the unknown crack path [8],[20]. Here, all cohesive surfaces act as potential crack paths to explicitly solve crack propagation specimens. The finite element mesh was generated with cross-triangular elements in a quadrilateral pattern as shown in Figure 1. This type of mesh gives the flexibility of resolving crack extensions with complex crack paths and minimal mesh-induced dispersion effects in the propagation of stress waves.

Lagrangian finite deformation formulation is used to account for finite strain at the crack tip regions. Weak formulation of the CFEM model based on the principle of virtual work with a contribution of cohesive surfaces is given by

$$\int_V \tau : \delta F \, dV - \int_{S_{int}} T . \delta \Delta \, dS = \int_{S_{ext}} T . \delta \mathrm{u} \, dS - \int_V \rho \frac{du^2}{dt^2} . \delta u dV \tag{1}$$

where $\boldsymbol{\tau}$ is the first Piola-Kirchoff stress, $\boldsymbol{F}$ is the deformation gradient, $\boldsymbol{T}$ is the applied traction, Δ is the surface separation on the material point of the cohesive surface. S_{ext}, S_{int}, and V are the external surface area, internal surface area, and volume of the body in the reference configuration. A plane strain condition was assumed. Elements pertaining to cohesive elements are governed by irreversible bilinear cohesive law for tensile separation whereas bulk elements are governed by Viscoplastic constitutive model as described in the next section.

2.2.2 Viscoplastic Constitutive model

Viscoplastic constitutive model in this study uses large deformation Viscoplastic theory described by David et. al [21]. Decomposition of deformation gradient in the viscoplastic model above is based on Gurtin et al [[22]. Finally, the constitutive model is set up based on rate-dependent model as described in the work of Weber et al. [23].

Position of a particle after deformation denoted by x_i is given by

$$x_i = F_{ij} X_j \tag{2}$$

Where **F** is the deformation gradient with respect to reference coordinate and X is the position before deformation.

Deformation gradient representing a vector from a reference state to the deformed configuration can be decomposed into elastic $\mathbf{F^e}$ and viscoplastic deformation gradient $\mathbf{F^{vp}}$ represented as a product of as

$$\mathrm{F} = \mathrm{F}^{\mathrm{e}} \cdot \mathrm{F}^{\mathrm{vp}} \tag{3}$$

Subsequently, F^e is a tangent vector obtained by pure elastic deformation and rotation whereas F^{vp} is obtained by pure plastic deformation and rotation.

Velocity gradient tensor **L** is given by the sum of rate of deformation **D** representing the symmetric part and material spin **W** representing the asymmetric part of **L** is given as

$$\mathrm{L} = \dot{F} \cdot \mathrm{F}^{-1} = \mathrm{D} + \mathrm{W} \tag{4}$$

D and **W** are defined by

$$D = \frac{1}{2}(L + L^T) \tag{5}$$

$$W = \frac{1}{2}(L - L^T) \tag{6}$$

$\dot{F}$ is a velocity coordinate given as follows:

$$\dot{F} = \frac{d\bar{v}}{d\bar{x}} \tag{7}$$

Considering all the above equations and substituting into velocity gradient L is given by,

$$L = \dot{F} \cdot \mathrm{F}^{-1} = \dot{F^e} \cdot \mathrm{F}^{\mathrm{e}-1} + \dot{F^{vp}} \cdot \mathrm{F}^{\mathrm{e}} \cdot \mathrm{F}^{\mathrm{vp}-1} \cdot \mathrm{F}^{\mathrm{e}-1} \tag{8}$$

where D and W can be decomposed into plastic and elastic components as

$$D = D^e + D^{vp} \tag{9}$$

$$\mathrm{W} = \mathrm{W}^{\mathrm{e}} + \mathrm{W}^{\mathrm{vp}} \tag{10}$$

Here, D^{e} refers to the elastic deformation rate from the theory of hypo-elasticity and constitutive relations. D^{vp} refers to the viscoplastic deformation rate under finite deformation given by the flow rule. Plastic strains are assumed to be much larger than elastic strains in the case of finite deformations. Separating elastic and plastic components of velocity gradient,

$$\mathrm{D}^{\mathrm{e}} + W^e = \dot{F^e} \cdot \mathrm{F}^{\mathrm{e}-1} \tag{11}$$

$$\mathrm{D}^{\mathrm{vp}} + W^{vp} = \dot{F^{vp}} \cdot \mathrm{F}^{\mathrm{e}} \cdot \mathrm{F}^{\mathrm{vp}-1} \cdot \mathrm{F}^{\mathrm{e}-1} \tag{12}$$

Strain ε is dependent on stress in terms of,

$$\varepsilon = \frac{1}{2}(F^T \cdot F - I) \tag{13}$$

$$\tau = C \cdot \varepsilon^e$$

For isotropic material, C, a fourth-order tensor is given by

$$\mathrm{C} = \frac{\mathrm{E}}{1+\nu}\left[\mathrm{I}' + \frac{\nu}{1-2\nu}\mathrm{I}\otimes\mathrm{I}\right] \tag{14}$$

Where E is Young's modulus, ***I*** is an identity matrix of order, and ν is the Poisson's ratio.
The plastic region is determined based on a yield stress function f. If the equivalent stress is greater than the yield function, the element is considered to be in the plastic zone. Definitions of

$$f = \sigma_{eq} - \sigma_y \tag{14}$$

Equivalent stress in yield function can be calculated as,

$$\sigma_{eq} = \sqrt{\frac{3}{2}\tau'_{ij}\tau'_{ij}}\ , and \quad \tau' = \tau - \frac{1}{3}trace(\tau) = \tau + p$$

Hydrostatic pressure required to calculate the equivalent stress is given by the Mie-Gruineisen equation of state from the procedure followed by Renaugh et al. [24] This equation is used to incorporate shock loading[3] in the CFEM framework.

$$p = K\phi + A\phi^2 + B\phi^3 + \gamma(1+\phi)e \tag{15}$$

$$\phi = 1 - \frac{\rho}{\rho_0} = \frac{1}{J} - 1$$

Where K is the bulk modulus, γ is the Gruineisen parameter, A and B are parameters obtained by fitting a Hugoniot curve, e is the internal energy per unit volume, and J is the Jacobian.

Parameters used in this study are given in the table 1.

If the mises yield function shows plasticity, where $\boldsymbol{f} < 0$, the following approach is used to determine Kirchoff stress at the next time step.

$$\tau_{ij(t+\Delta t)} = \tau_{ij(t)} + \dot{\tau} \cdot \Delta t \tag{16}$$

Where $\dot{\tau}$ is the stress rate given by

$$\dot{\tau} = \hat{\tau} - \mathrm{W} \cdot \tau + \tau \cdot \mathrm{W} \tag{17}$$

Based on linear form of hypoelasticity, Jaumann rate of Cauchy stress is used in this work. Material spin $\boldsymbol{W}$ consists of plastic and elastic part. *From* flow rule of large deformation in the case of isotropic hardening solid[26], D^{vp} is given by

$$D_{ij}^{vp} = \frac{df}{d\tau_{ij}}\dot{\lambda} = \tau'_{ij}\dot{\lambda} \tag{18}$$

where *f* is the yield stress function, $\dot{\lambda}$is the effective viscoplastic strain rate.

$$\dot{\lambda} = \frac{3}{2}\frac{\dot{\bar{\varepsilon}}^{vp}}{\sigma_{eq}} \tag{19}$$

$$\bar{\varepsilon}^{vp} = \chi\left(\dot{\bar{\varepsilon}}\right)^{m}(\bar{\sigma})^{n} \tag{20}$$

Kirchoff's stress consists of deviatoric $\hat{\tau}$.and dialation part. Dialation part p is calculated by eq(15). Time rate of deaviatoric part of Kirchoff's stress is given by $\hat{\tau}$. The viscoplastic spin rate is equated to zero under the assumption that the material is in a non-spinning relaxed configuration [27],

$$\hat{\tau} = \mathrm{C} \cdot \mathrm{D}^{\mathrm{e}} = \mathrm{C} \cdot (\mathrm{D} - \mathrm{D}^{\mathrm{vp}}) \tag{21}$$

Cohesive zone parameters used in this study are obtained from previous experimental data for HMX-HTPB microstructures [7] are shown in table 2.

2.2.3 Cohesive Surface-Irreversible Bilinear Cohesive Law

Separation of cohesive surfaces is governed by irreversible bilinear cohesive law for tensile separation describes effective instantaneous state of mixed-mode separations [14], [28]. Traction applied on a cohesive surface is given by the work-conjugate to interfacial separation Δ. It is assumed that the separation in the surfaces define cohesive traction.

$$T(x) = T[\Delta(x)] \tag{22}$$

Calculations presented here are from the work of Zhai et. al [14] on bilinear traction separation law as described with a state variable as,

$$\lambda = \sqrt{\left(\frac{\Delta_n}{\Delta_{nc}}\right)^2 + \left(\frac{\Delta_t}{\Delta_{tc}}\right)^2} \tag{23}$$

where n and t represent the tangential and normal components to interfacial separation. Δ_c corresponds to critical separation value at which strength of the cohesive surface vanishes under pure normal and shear conditions.

Irreversibility of separation is described by a parameter η which obtains the maximum value of stiffness at initial undeformed state (η_0) and maximum value of λ representing unloaded stiffness of cohesive surface after damage as shown in Figure 2

$$\eta = max\{\eta_0, \lambda_{ul}\} \tag{24}$$

A relation between cohesive surface separation and traction is given by surface energy dissipation per unit area Φ.

$$\Phi = \Phi(\lambda, \eta) = \begin{cases} \Phi_0 \left(\frac{1-\eta}{1-\eta_0}\right)\left(\frac{\lambda^2}{\eta}\right), \text{ if } 0 \le \lambda \le 2 \\ \Phi_0 \left(\frac{1-\eta}{1-\eta_0}\right)\left(1 - \frac{(1-\lambda)^2}{1-\eta}\right), \text{if } \eta \le \lambda \le 1 \end{cases} \tag{25}$$

Based on the work-conjugate of Δ in the above eq(22),

$$T = \frac{d\Phi}{d\,\Delta} \tag{26}$$

Shear and normal components of traction are given by T_n and T_t

$$T_n = \sigma(\lambda, \eta)\frac{\Delta_n}{\lambda\Delta_{nc}} \tag{27}$$

$$T_t = \sigma(\lambda, \eta)\frac{\alpha\,\Delta_t}{\lambda\Delta_{tc}} \tag{28}$$

Where $\alpha = \frac{\Delta_{nc}}{\Delta_{tc}}$ and σ is given by

$$\sigma = \sqrt{(T_n)^2 + \left(\frac{T_t}{\alpha}\right)^2} = \begin{cases} \left(T_{max}\dfrac{1-\eta}{1-\eta_0}\right)\dfrac{\lambda}{\eta} & \text{if } 0 \le \lambda \le \eta \\ \left(T_{max}\dfrac{1-\eta}{1-\eta_0}\right)\dfrac{1-\lambda}{1-\eta} & if\ \eta \le \lambda \le 1 \\ 0 & if\ \lambda > 1 \end{cases} \tag{29}$$

Work per unit area from normal and shear tractions in eq(27, 28) can be calculated by the integral given below at any stage of deformation.

$$\int_0^{\Delta_c} T.\,d\Delta = \frac{1}{2}T_n^{max}\Delta_{nc} = \frac{1}{2}\alpha T_t^{max}\Delta_{tc} = \Phi(1, \eta_0) = \Phi_0 \tag{30}$$

Variation of surface energy dissipation is described as equations below with four conditions based on values of λ. Last condition where $\lambda > 1$ surfaces are fully separated. A sum of dissipated energy from all cohesive surfaces after deformation is equal to the total dissipated work.

$$\Phi_d(\lambda, \eta) = 0, \qquad if \lambda > \eta_0$$
$$= \Phi(\eta, \eta_0) - \phi(\eta, \eta) = \frac{\eta - \eta_0}{1 - \eta_0}\Phi_0, \qquad if\ \eta_0 \le \lambda \le \eta$$

$$= \Phi(\lambda, \eta_0) - \phi(\lambda, \eta) = \frac{\lambda - \eta_0}{1 - \eta_0}\Phi_0\,, \qquad if\ \eta \le \lambda \le \eta$$

$$= \Phi_0, \qquad if \lambda > 1 \tag{31}$$

Penalty traction is applied in case the normal component of $\Delta<0$ to avoid any interpenetration of cohesive surfaces.

$$T_n = T_n^{max} exp\left(\frac{\Delta_n}{\Delta_{nc}}\right), \qquad for\ \Delta_n < 0 \tag{32}$$

Current temperatures are calculated using temperature change as described below, where T_{ref} is the reference temperature and considered to be the room temperature.

$$T\ =\ \Delta T + T_{ref} \tag{33}$$

Change in temperature ΔT is calculated using internal energy per unit volume, density ρ at deformed state, and heat capacity at constant pressure c_p. Values for heat capacity are shown in table 3.

$$\Delta T = \frac{e}{\rho c_p} \tag{34}$$

$$e = S_{ij}\varepsilon_{ij} \tag{35}$$

where S and ε represent stress tensor and Lagrange strain tensor respectively. These two values are obtained from simulations.

2.2.4 Modeling of Impactor Shapes – Spherical and Planar

The cohesive finite element method (CFEM) framework was implemented using a SI and a SI. Compressive deformation from the impactors was applied to the samples. A SI is an idealized sphere of a radius much larger than the dimensions of the sample such that the stress wave it propagates is one-dimensional. On the other hand, a SI [29] is a point from which the wave spreads radially. The larger the radius of the sphere, the closer it would be to the SI.

In the case of a SI, all the top nodes of the specimen were chosen, and velocity in the negative y-direction was given such that it acts as a SI. To model an impactor shaped like a sphere, one of the two methods can be used. In the first method, nodes placed at the top of the specimen could be picked, varying with time-based on an equation describing the circumference of the circle. However, it would require a close form solution for shear and normal stress at this boundary. The second method is to use a material (buffer) in between the impactor and sample to allow for a spherical wave formation as shown in Figure 3. The diameter of the impactor decides the impact length as well as the height of the material. The radius of the impactor was chosen to be greater than the particle size in any microstructure used in this study.

The second method proved to be useful even though it involved more elements in solving for and longer computational time. Determination of material properties of buffer material was important to transfer most amount of pressure from the impactor to the sample. The density of the impacting material and the impacted material determines their ability to propagate stress waves [30]. With an impedance mismatch between the two layers, there would be a reflection of stress waves at the interface of the two materials. With HMX crystals having a higher impedance, the maximum density value that could be used to propagate most of the pressure was to use its properties for the buffer. As propagation of waves involves some forms of losses [31], for comparison of the SI and SI, pressure profiles had to be matched for velocities that were used.

Verification of SI

To verify the impactor model proposed with the real impact with spheres, explicit dynamic Abaqus models were set up. First model consisted of a specimen of height and width of 0.1mm with a SI of required radius. The second model consisted of specimen size of same dimensions with a buffer material to transmit the impact wave as a spherical wave. Impactor used here was a flat impactor of same size as the diameter of the impactor. First few time steps till the wave reaches the specimen were simulated before the stress wave gets reflected within the buffer material due to the difference in impedances of the material.

Abaqus models with their boundary conditions can be seen in Figure 4 with plane strain condition. Both spherical and SIs were given similar boundary conditions. The sides of the specimen were applied with x-symmetric boundary condition whereas the bottom of the specimen was restricted in y direction. An impact velocity of 10m/s was applied in the y-direction for SI with

equivalent impact velocity for SI. Mesh size of 0.001 was used for the analysis. Material properties of the sample was chosen as used for CFEM analysis but with composite properties approximated to be 60% crystal with 40% binder. Contact properties were defined between the impactor and the top boundary of the sample with kinematic surface to surface contact. Tangential with frictionless and normal behavior with hard contact were defined.

Velocity profiles of SI describes the wave fronts of the two are comparable as shown in Figure 6. Before impact, as the stress wave moves through buffer material, the radius of the wave expands, forming a similar wave front as that of a SI. Even though in the velocity profile, the time at which SI was captures was way after that of the equivalent model, it forms a similar wave front which expands as it moves into the sample. Once the stress wave moves through the buffer material, only a part of it moves into the sample due to material impedance mismatch and the rest of it gets reflected into the buffer material. This reflected wave creates another stress wave with an addition of impact wave, creates a ripple as the time progresses. Thus, it was necessary to limit the usage of buffer material model to initial stages of impact in CFEM analysis.

Pressure Matching

To find the velocity needed to be applied to the SI to match a particular velocity in planar, pressure on impact was matched at the mid-section, just beneath the impact was matched over time in both cases. In Figure 5, pressure matching for 0.1m/s velocity is shown. In the specified velocity profile, for a specified velocity of planar impact, double the velocity on spherical impact is used. This is specific to the impactor radius of 0.25mm with a buffer of 0.5mm.

Similar pressure matching was used for other planar impact velocities (0.5m/s, 1m/s, 5m/s, 10m/s) used for the analysis in this study. In the next sections of this report, impact velocity refers to the planar equivalent velocity in spherical impact. The rectangular mesh size containing four cross-triangular elements was 5μm, creating a 50x50 mesh matrix for a model size of 250μm x 250μm in planar impact whereas 50*50 mesh matrix for a model size of 300μm x 250μm in spherical impact.

Generated meshes are shown in Figure 7 as diamond microstructure, Figure 8 as PBX microstructure, and Figure 9 as circular particle microstructure.

A mesh convergence study was carried out to determine the size of the bulk elements of HTPB and HMX. as shown in Figure 10 A mesh size of 5μm was chosen for this study. Though a smaller value of mesh size could be chosen for a more independent simulation value of equivalent

stress, it would dramatically increase the computation time in spherical impact with 20% more elements from buffer material.

2.3 Results and Analysis

2.3.1 Validation

The maximum pressure of spherical impact from current work was compared to the experimental results from Dhiman et al. [32]. Here, HTPB with HMX crystal-based PBX was impacted with 250μm zirconia sphere impactor. Pressure distribution in the first 75ns of the impact was plotted at various particle velocities. CFEM simulations were run for different velocities for comparison. Figure 11 shows a plot of particle velocity with maximum pressure where a close match between experimental data and simulated data can be seen validating the used CFEM model.

2.3.2 Comparison with Equal Impact Velocities without Equivalent Model

To understand the importance of applying pressure matching in order to model SIs, equal impact velocities were applied to the SI with buffer as well as SI. Concept of equivalent velocities was disregarded and pressure (Figure 12), stress (Figure 13a) , and temperature(Figure 13b) distribution in the sample were plotted at different time steps. As observed from these plots, shock waves were not transferred completely into the specimen through the buffer. Buffer being made out of a material with higher impedance, due to impedance mismatch, the entire stress wave is not introduced into the specimen in case of SI. This is clearly observed with higher stress contours in the case of SI in comparison to SI. At lower time steps, the difference is not very apparent. But with time, planar impact has higher values. Temperature and stress distribution plots helps observe much higher average values in case of SI as a part of the stress wave is reflected back within the buffer material.

It is necessary to set a comparison criterion for the two impactors in order to gain understanding of various mechanisms involved in initiations in these materials. Pressure is used as a comparison criterion to set up an equivalent spherical model. Pressure matching at the point right below impact was used for further analysis to study microstructure effects.

2.3.3 Simulation Results

Initiation characteristics of EM can be varied by changing the morphology of the crystal. Delaying initiation by introducing other materials [16] and including fine-coarse grains in the microstructure [33] has been studied previously. The effect of the size of the particles on impact sensitivity has been studied by Manner et al. [34] experimentally. Properties of polycrystalline β-HMX without orientation dependency are used to model the specimens. Crystal morphology in energetic material plays an important role. Crystal morphologies used in this study are given in Figure 14 and Figure 15.

The current study carried out focused on two kinds of microstructure. Effect of alignment of force chain, particle shape and size with the influence of velocity is studied with a PBX microstructure from an earlier study [19] as shown in Figure 15. This microstructure was chosen due to the random placement of crystals with multifaceted irregular shapes, as in the case of PBX composites.

In the next part of the study, idealized microstructures from Zhou et al. [2] were considered to study the effect of microstructure on failure properties. It consisted of circular and rectangular-shaped crystals with varying volume fractions of 40%, 60%, and 80%, as shown in the Figure 14.

All simulations used the boundary conditions as described in Figure 16. In spherical and planar impact, the side boundaries were fixed in the direction perpendicular to the load. The bottom side of the sample is fixed in the direction of the load. The top side is loaded with uniform compressive loading for planar impact, whereas for spherical impact, the impact of a circular-shaped body with time is mimicked for a certain radius of the sphere.

Viscoplastic parameters m, n, and χ were obtained from work of Olokun et al. [35] as shown in table 4. Experimental data from impact test were plotted on stress-strain curves to fit Viscoplastic strain power law model. Slope, intercept, and power from the graph were obtained to determine the Viscoplastic parameters.

PBX microstructure

Digitized PBX microstructure was used for this study to observe propagation of stress waves in PI and SI. Maximum principal stress at t=60ns is plotted in Figure 17. With the main focus on the difference in the evolution of stresses in the initial stages of impact, maximum principal stresses in

samples were captured during the loading rise time of impact. A low impact velocity of 0.1m/s was considered. Due to the morphology of the PBX structure and orientation of crystals, the formation of force chains is observed with impact. In a granular material, most of the crystals carry less than average stress, called a weak-grain network. Stronger-grain networks form the indicated force of chains in the microstructure.

Grains in the marked (red arrows in the figure 17) force chains are more stressed than others showing assemblies of force chains—such grain assemblies in the sample support high compressive and shear forces from impact [36]. Higher stresses are sustained by HMX crystals due to higher material stiffness of HMX crystals in comparison to HTPB. With a sample size comparable to the size of the impact, the planar impact can form a more extended force of chains through the length of the specimen. With spherical impact, spherical stress wave formed in the structure plane of movement of waves gives a shorter path for the dissipation of stresses within the sample. Stresses increase till a failure mechanism like a trans granular fracture or interfacial debonding is initiated in the microstructure.

Figure 18 shows a plot of stress in the loading direction for two different time steps along the lateral section of the specimen. It highlights probed sections for normal stress with a box in` both modes of impacts. A specific section of the microstructure is chosen to focus on varying stress patterns. Point A corresponds to the interface phase of HMX-HTPB. Position B corresponds to HMX crystal. Region in between A and B packs mostly the binder with small sized HMX crystals.

Maximum normal stress in planar impact occurs at the interface. In spherical impact (SI), maximum stress occurs inside the crystal. Increased interaction between the HMX-HTPB interface and large crystal stress concentration might be the cause of high stresses in PI [16]. At t= 60ns in spherical impact, a lower pressure wave is observed around the sides of the distribution along X. In planar impact, the distribution is more uniform. With activation of other force chains, stress concentrations might not Initially, both the impacts have fairly similar stress at the lower time of 60ns. There is a slight peak in planar impact at point A. After 270ns, stresses peak corresponding to closely packed small particles before A and after B. Peak variation is higher in spherical impact due to the number of force chains involved in transmission of forces. In PI, the primary force chain consisting of majority of large particles of HMX on the left side of the sample is involved. No crystals in between A and B points are activated with time in PI. But some of the force chains pass through this zone giving a variation of stresses. Average stresses are higher in SI but variance is

higher in PI. With time, a possibility of reflection of stress wave from the boundaries on the sample could be observed.

Increased shear stresses can be a factor to be considered to determine failure due to impact [37]. Shear stresses at interfaces increase the temperature of the surrounding medium rising the temperature leading to possible hotspots. Comparison of shear stress in the sample between PI and SI gives a good understanding of the possibility of hotspots, leading to deflagration or detonation of energetic materials. Shear stresses are plotted in Figure 19. Even though the velocities for both the samples were the same, higher shear stresses along the boundaries can be observed in spherical impact. Initially at time 60ns, similar stresses can be observed. With time, higher shear stresses in SI can be observed. Based on the chosen set of crystals for force transmission in each kind of impact, shear stresses around them develop. Based on the shear stress contour plot, higher shear stresses can be observed around the impact region of SI suggesting SI can be more prone to failure with tightly bonded crystals.

In Figure 20, a temperature distribution is plotted. According to criteria for hotspot formation as discussed in a previous work [10], a temperature of a minimum of 700K is necessary. In SI, just below the point of impact, the temperature reaches to about 1000K. This might be due to the concentration of force due to the nature of the impact. Temperature rise is more uniform in the binder of PI in comparison to SI. Temperature rise in SI move into the grains from the binder faster in SI in comparison to PI.

Time dependent equivalent stress profiles in Figure 21 show impact behavior in HMX-HTPB samples in SI and PI. Evolution of stresses in crystals as well as the binder can be observed from a lower to a higher time step. On the top row, stresses in the binder are plotted with time stamps of each marked. On the lower row of the stress distribution plot, crystals in the microstructure are plotted. In both SI and PI, the stresses propagate into the crystals faster than the surrounding binder. Stress within the grains are higher and concentrated at the midpoint of the specimen in the case of SI in comparison to PI. At lower time steps, the difference is not much for difference in impactors for binders. It is more pronounced in grains where SI shows a higher value.

Maximum equivalent stresses were plotted for various other velocities of 0.5m/s, 1m/s, 5m/s, and 10m/s as shown in Figure 22. Higher stresses can be observed in SI in comparison to planar impact at all the plotted data points. Difference in maximum stress between PI and SI increased with higher impact velocities. A possible cause might be the increased concentration of pressure with

velocity around the region of impact leading to stress concentrations. These regions could be observed in shear stress plots and temperature rise plots.

Idealized microstructures

Effect of crystal shape and volume fraction was analyzed by impacting two sets of idealized microstructures. First set consisted of circular crystals, representing rounded edge crystals. Diamond-shaped crystals were selected with different sizes were selected to simulate detonator-grade crystals with sharp edges. These angular edges of the crystal create a higher number of hotspots in comparison to rounded edges. Volume fractions of 40%, 60%, and 80% were used.
Figure 23 shows the equivalent stress profiles in a rectangular particle microstructure.

Like the evolution of stresses described in digitized PBX microstructure, similar force chains for stress propagation can be seen in rectangular and circular microstructures as shown in Figure 23. The stress profile generated was developed from 80% volume fraction of rectangular microstructure at an impact velocity of 1m/s. At the same time step, SI has as higher stress concentration at the point of impact. The pressure wave gets localized onto the interface of HMX-HTPB interface. With higher impact velocities, pressures increase, due to an impedance mismatch between the grain and binder, wave reflection takes place at the HTPB-HMX interface creating a concentration of stresses which might lead to a possible delamination. This phenomenon is wave reflection at the interfaces can be observed as the volume fraction of the grains is increased with circular and rectangular microstructure. An impact velocity was applied to the top nodes for SI and PI of the circular microstructure with varying volume fraction. Equivalent stresses are plotted in Figure 24. From the equivalent stress plot, it can be observed that the overall stresses increase as the volume fraction increases. Largest crystals can be located in 60% volume fraction. With larger crystals, higher stress concentrations can be seen.

With larger crystals, higher stress concentrations can be seen. The same crystals in Figure 28 around the edges have a higher temperature in comparison to smaller crystals. These crystals tend to form a stronger network for force propagation in the samples. Though similar routes for propagation of stresses were chosen (Figure 24) in SI and PI at 60% volume fraction, two other minor paths are also highlighted. These highlighted paths have more concentrated contours in SI in comparison to PI. In 40% volume fraction microstructures, the stress dispersion between spherical wave and planar wave can be seen in both Figure 24 and Figure 25. For PI the distribution of stress is uniform around

the binder and crystal for planar, even though stress wave tends to travel through crystals. In case of a SI, red dots can be notices around large crystals at the top which are closely packed other crystals. The interface between the two seems to undergo higher stresses. The resulting temperature for both these impacts can be observed. In PI, the temperature rise is uniform through the binder but there are pockets of high stress regions exist in SI. In the case of 80% volume fraction, left most region in planar impact is most stressed for a PI. This region consisted of large crystals which were closely packed. The same force chain is not chosen in SI. Instead, stress contours projecting outwards are noticed.

With longer simulation time, reflection of these stress waves from the walls can be seen. These stresses regions in PI can be seen as a temperature rise between interfaces on the left. SI takes a cone shaped propagation region. Grain arrangements falling outside this region do not seem to get affected. The angle of this cone is dependent on the size of the SI. Smaller the size, smaller is the propagation wave cone angle. Another observation from the temperature plot is that for a SI, the temperature profile is not very uniform. There are high temperature concentration regions in the direction of propagation around the crystals they are packed closest.

Rectangular microstructures with 40%, 60%, 80% of volume fractions are subjected to compressive loads from PI and SI to obtain stress profiles in Figure 25. At 40% of volume fraction, HMX-HTPB interfaces are highlighted in both SI and PI. With an increase in the volume fraction, right below the point of impact, at the mid-section of the specimen, a high stress concentrated zone is seen to develop.

Normal stresses from each kind of microstructure for all considered volume fractions were plotted from the same point within the crystal to observe the reach of stress wave in PI and SI. Figure 26 shows a plot of normal stress with time for rectangular microstructure. In the plot, spherical impact is denoted by dashed lines and planar with solid lines. All the planar impact and spherical impact curves form two groups in the plot. SI shows a higher normal stress inside a crystal compared to spherical ones. This might be due to more dispersion of stress wave in the upper portions of the sample in SI as seen in equivalent stress plots. Higher the volume fraction, greater is the normal stress in case of planar impact. But 60% volume fraction of SI tops the curve in comparison to other spherical impacts. Though the same crystal was picked in all these rectangular microstructures, there could be a possibility of the chosen crystal not being in the force chain for highest volume fraction in spherical impact. The chosen force chain in planar condition was the same in all volume fractions

but spherical was not. Thus, path determination of force becomes more complex with spherical impact. Lowest stress in both the cases is in 40% volume fraction microstructure showing a decrease in stress with lower volume fractions.

Figure 27 shows a plot of normal stress with time for circular crystal microstructure. Like the rectangular microstructure described above, the circular microstructure was plotted. Unlike rectangular microstructure, there was no grouping of different impactors. Overall stresses in comparison to rectangular microstructure were higher in the circular microstructure. This might be due to more transfer of forces in rectangular microstructure in comparison to circular. Overall stress when SI and PI are compared shows higher stresses in PI. At 80% volume fraction, SI in the initial stages is slightly lower than PI, but at about 200ns, it overtakes PI. Higher particle volume fraction has higher stresses in the case of circular microstructure in both impactors. Force chain not being the same might be a reason for 40% volume fraction being on the lower end of the spectrum in the case of SI. As the crystals are packed closer, determining a strong network for transmitting force becomes a factor affecting the likelihood of failure in a specimen.

2.3.4 Applications of Current Study

In the current study, differences between spherical and SI are discussed with various effects such as force chain effect, crystal shape effect, and crystal proximity which can be broadly categorized as microstructural effects. These effects tend to be more pronounced as the impact velocity increases as seen in rate effects analyzed in the current study.

Understanding such effects at smaller impact velocities would be extrapolate it to larger velocities in experimental studies such as in the work of Dhiman et al. 2021 [32]**.** Here, shock wave propagation is analyzed in HTPB-HMX samples with a SI made of Zirconia at high impact velocities of around 225-543m/s. This study also compares pressure distribution between planar and spherical impact which highlights a large dip in pressures with time in comparison to planar impact. Though the maximum pressures are comparable, SI has slightly higher pressure. Such a comparison is adopted in the form of pressure matching criteria used for equivalent spherical model. This comparison can be seen in figure 28.

With an expensive, complex, and time-consuming experimental setup, it is difficult to perform experiments for a large range of impact velocities to understand initiation better. It is highly important to understand various effects that affect initiation and be aware of it while performing

experiments. Computational analysis would aid well with experimental results to understand various mechanisms as it offers a spatial distribution of temperature rise, stresses, as well as pressures which might be a limitation with experimental set up. One such effect previously predicted by computational studies [17] was the interface effect where stress around the interfaces were higher. This phenomenon was again discussed in [32]. At such high impact velocities, the SI does not behave rigidly which is shown in the shock pressure distribution from the experimental studies. Using a non-rigid impactor would give more accurate results with CFEM simulations. Thus, this study provides a good insight on the microstructural effects affecting mechanisms of initiation in energetic materials.

2.4 Conclusion

In this work, the role of impactor shapes in energetic materials was analyzed to understand failure mechanisms in different microstructures. Two shapes of impactors were modeled for CFEM framework-based impact analysis. For SI, compressive load was applied directly on the nodes. SI used a buffer material in between the impactor and the sample to mimic an impact from a sphere. To obtain the same force of impact on both impactors, pressures at the point of impact were matched.

Two categories of microstructures were used for this analysis. In digitized PBX microstructure, maximum stress profile highlighted activation of different force chains consisting of large grains with impact. SI consisted of radially outward force chains propagating the impact whereas planar impact consisted of force chains moving towards the bottom of the sample. Both the force chains were in the direction of the impact surface.

Normal stress profile and shear stress profile plots over different time steps showed the evolution of stresses around interfaces. SI showed higher number of shear stress concentration regions around the interfaces which could be a possible cause for delamination fracture in these energetic materials. In spherical impact, a drastic jump in the shear stress level was seen from a lower to higher time stamp whereas a more subtle stress jump was seen in planar impact. A similar observation was made with normal stress profile distribution. It also emphasized higher number of force chains involved in spherical impact for the propagation of same pressure. Stresses around the boundaries of the crystal evolve faster with time in both kinds of impacts but stress concentrations are higher in case of spherical impact. Spherical impact showed development of more points with

temperatures reaching critical hotspot temperature. As the impact velocities were increased, the difference between maximum stress levels of spherical and planar impact increased.

Circular and rectangular shaped different shapes with different volume fractions were used for impact induced failure. Similar force chains as witnessed in PBX microstructure was observed in these microstructures. It was observed that SI and SIs use different grain networks for force transmission. Depending on the radius of the impactor, grains on the upper corners of a sample do not affect the initiation reaction of energetic materials. Increased volume fraction resulted in higher stress levels both kinds of impactors. But on an average, spherical impact had lower normal stresses in comparison to planar which might be caused by multiple force chains that were seen on equivalent stress profile. Circular impact at 60% volume fraction had a higher stress due to the large crystal sizes.

Based on all the observations from the analysis hotspot formation in SI right below the impact region is higher in SI due to the concentration of forces into a small region. Temperature profiles show higher than critical temperature required for hotpots at these regions in SI.

2.5 Table and Figures

Table 1: Mie Gruneisen parameters for HMX [25]-HTPB [24] samples

Material	K (10^2GPa)	A (10^2GPa)	B (10^2GPa)	γ	ρ_0 (g/cm^3)	E (MPa)	ν
HTPB	0.02	0.294	0.0196	0.7	0.9	2.5	0.45
HMX	0.125	0.22	0.15	1.03	1.9	14240	0.31

Table 2: Cohesive zone parameters from previous experimental data [7]

Material	Cohesive Strength (MPa)	Critical displacement (mm)	Cohesive energy (kJ/m^2)
HTPB	0.8	0.5	0.2
HMX	100	5×10^{-3}	0.25
HTPB-HMX interface	1.6	0.16	0.13

Table 3: Heat Capacity for HMX and HTPB

Material	Heat Capacity (kJ/kg K)
HMX	2.5
HTPB	0.975

Table 4: Viscoplastic material properties based on experimental results [35]

Parameter	X (MPa) $^{-n}$	m	n
HTPB	0.54	-0.18	1.78
HMX	1.08	-0.79	1.58
HTPB-HMX interface	1.59	-0.87	1.88

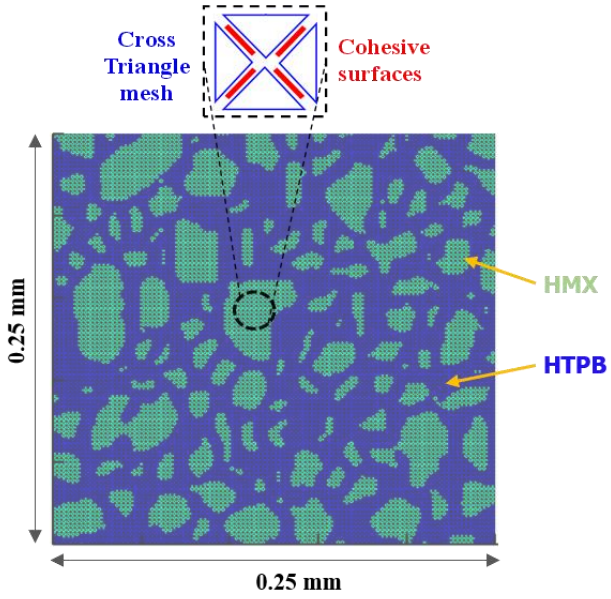

Figure 1:Mesh and model specifications

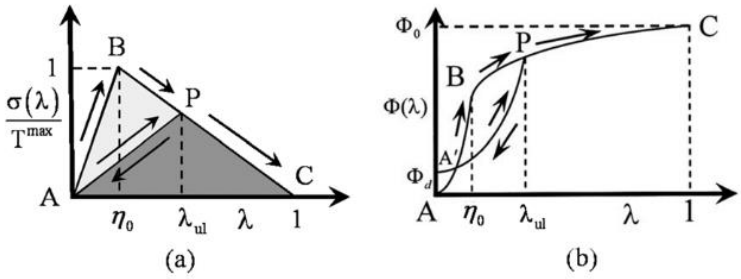

Figure 2: Irreversible Bilinear cohesive law

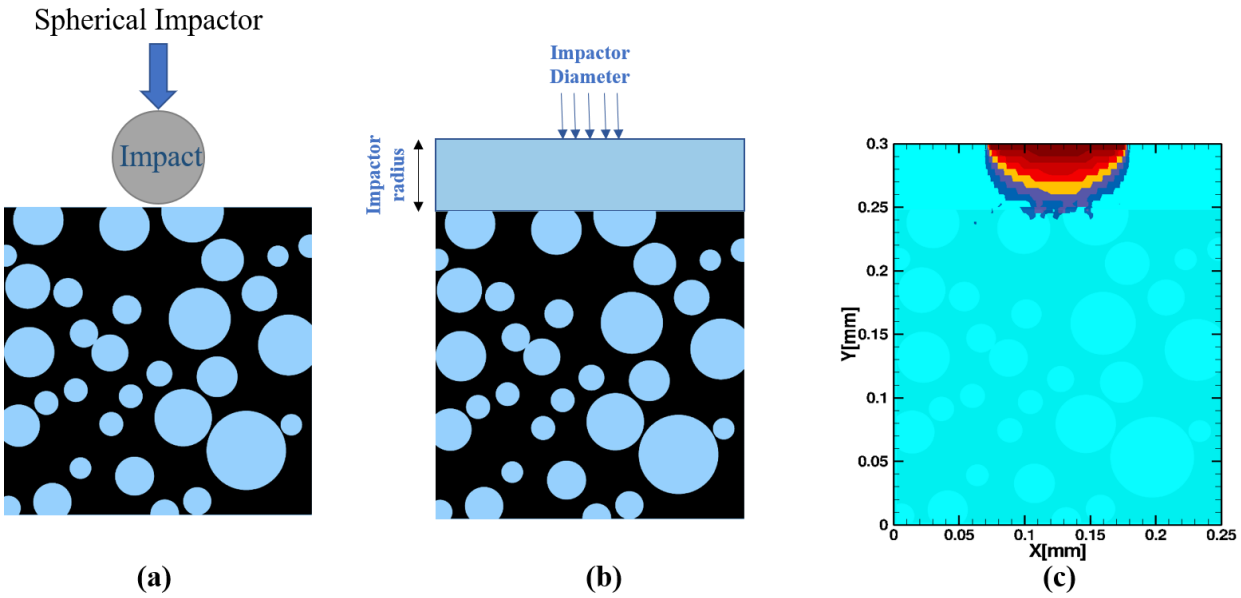

Figure 4: Spherical Impact model a) Impact condition b) Applied model c) Simulation.

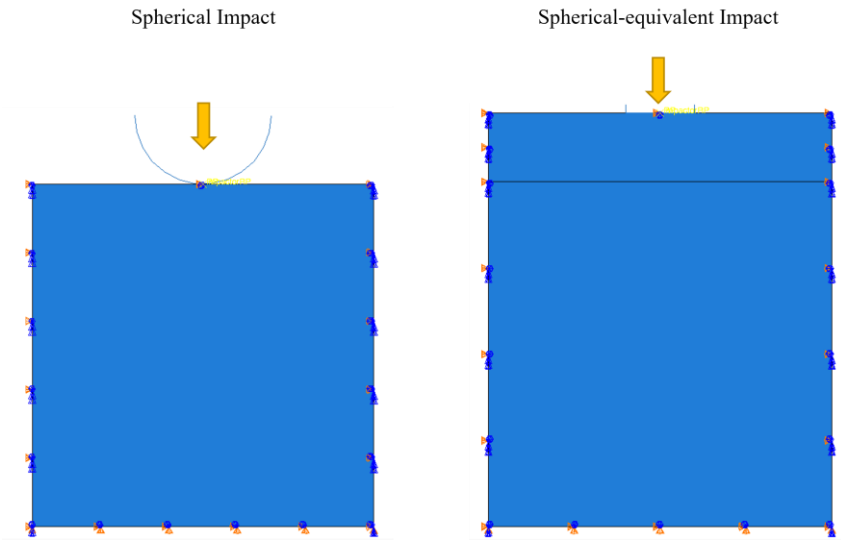

Figure 3: Abaqus model with boundary conditions

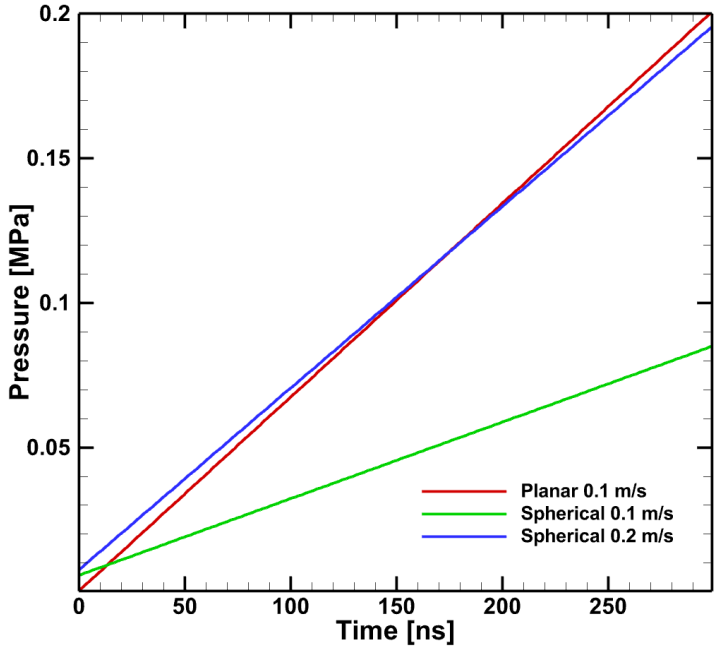

Figure 5: Pressure matching for 0.1m/s velocity for spherical impactor

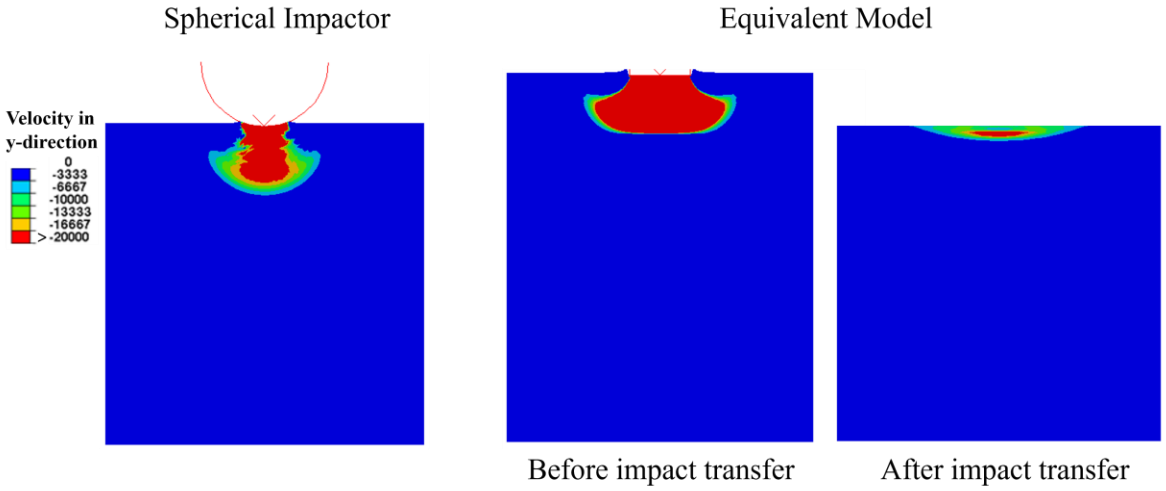

Figure 6: Velocity profile in spherical and Equivalent spherical model

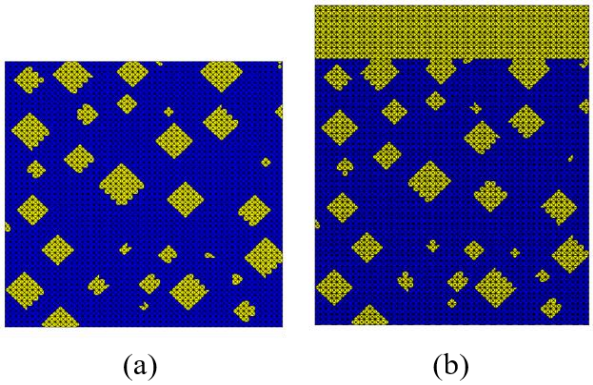

Figure 8: Generated diamond microstructure a) Planar b) Spherical impact specimen

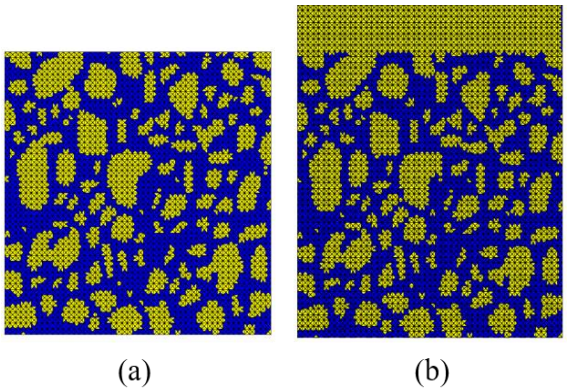

Figure 7: Generated mesh for PBX microstructure a) Planar b) Spherical impact specimen

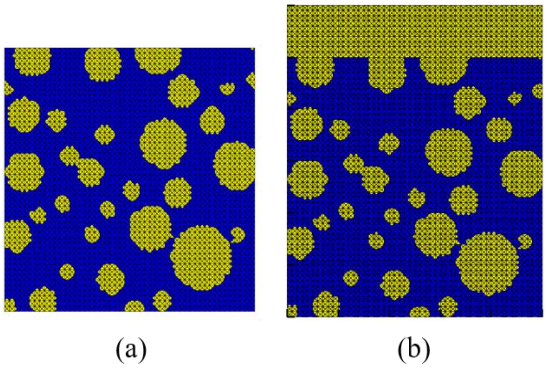

Figure 9: Generated circular microstructure a) Planar b) Spherical impact specimens

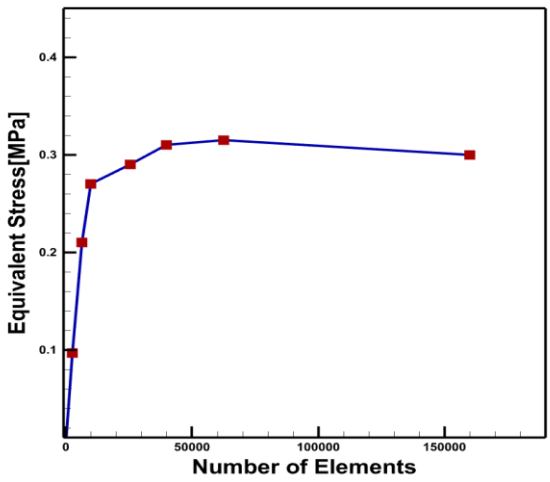

Figure 10: Mesh Convergence

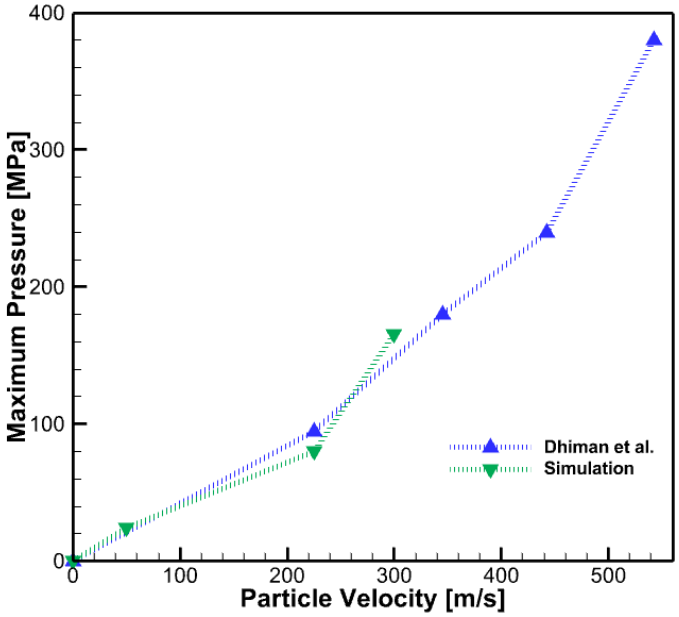

Figure 11: Comparison of pressure obtained from experiment [32] at various velocities

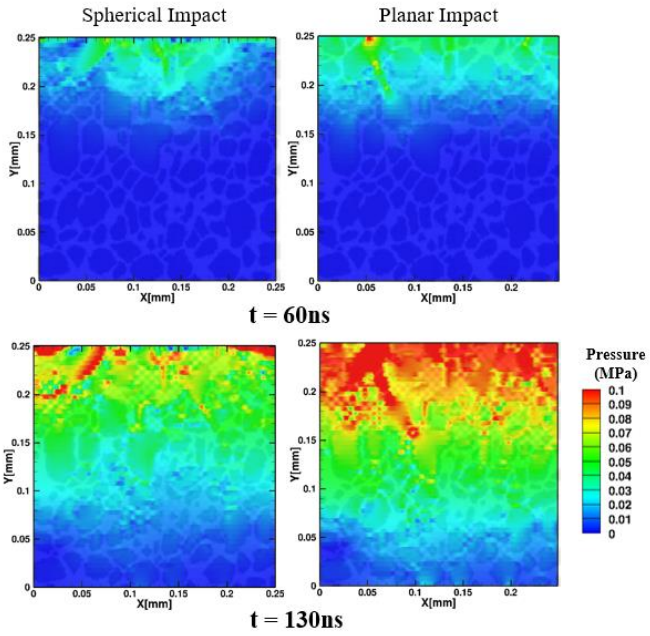

Figure 12: Pressure Distribution without Equivalent Model

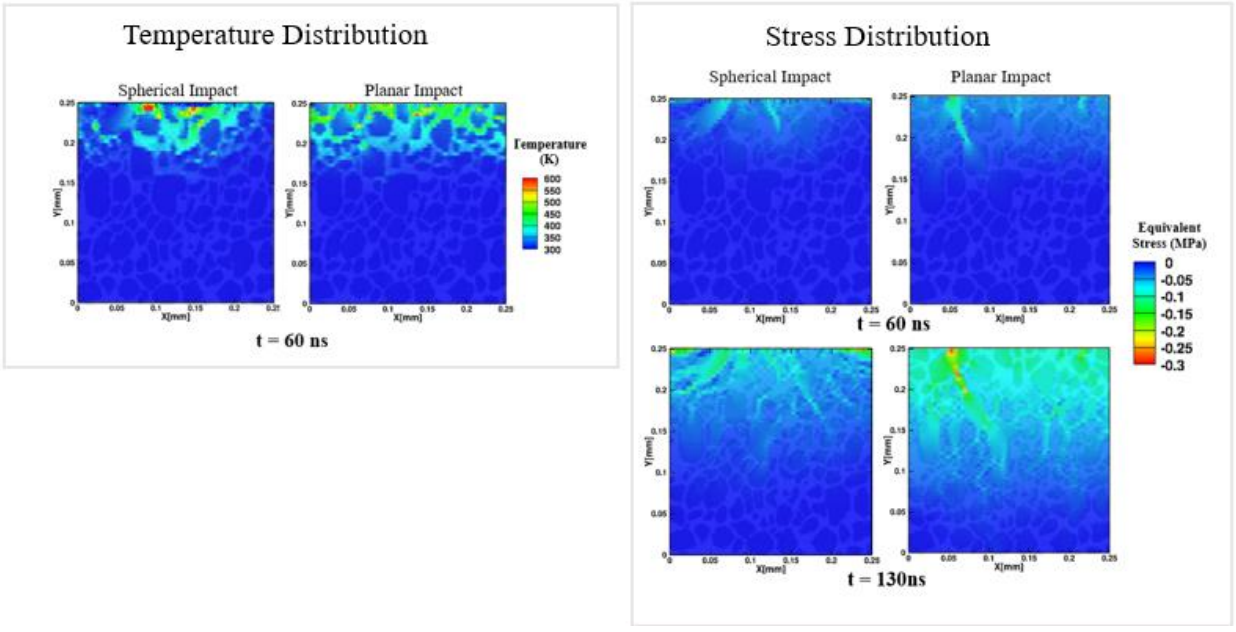

Figure 13: Temperature and Stress Distribution in spherical and planar impactors

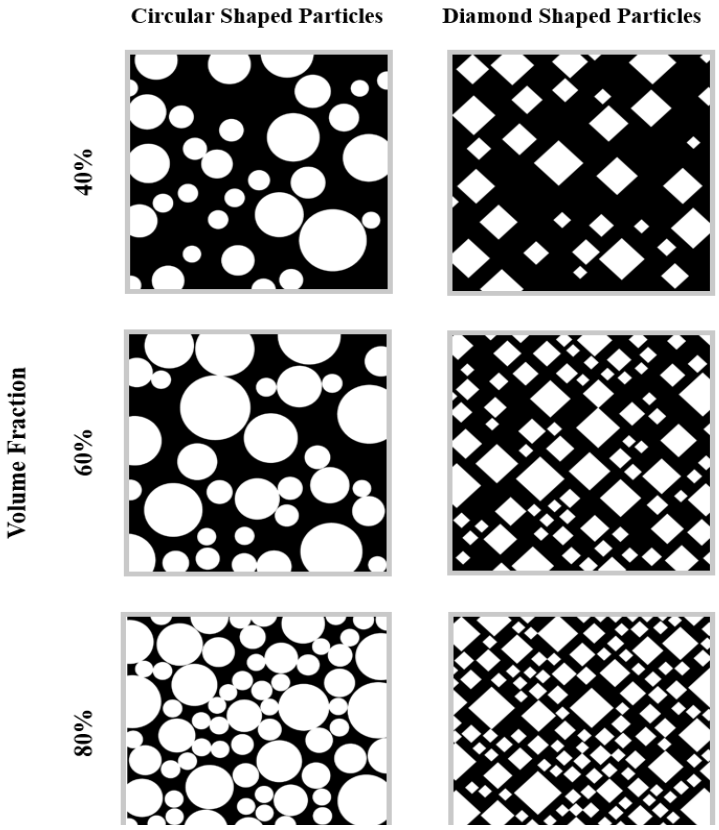

Figure 14: Idealized microstructures used in the simulation

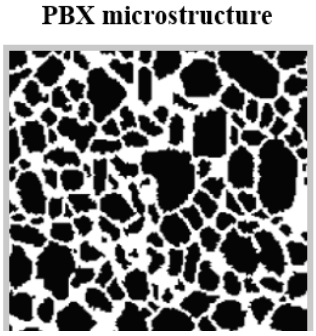

Figure 15: Digitized PBX microstructure

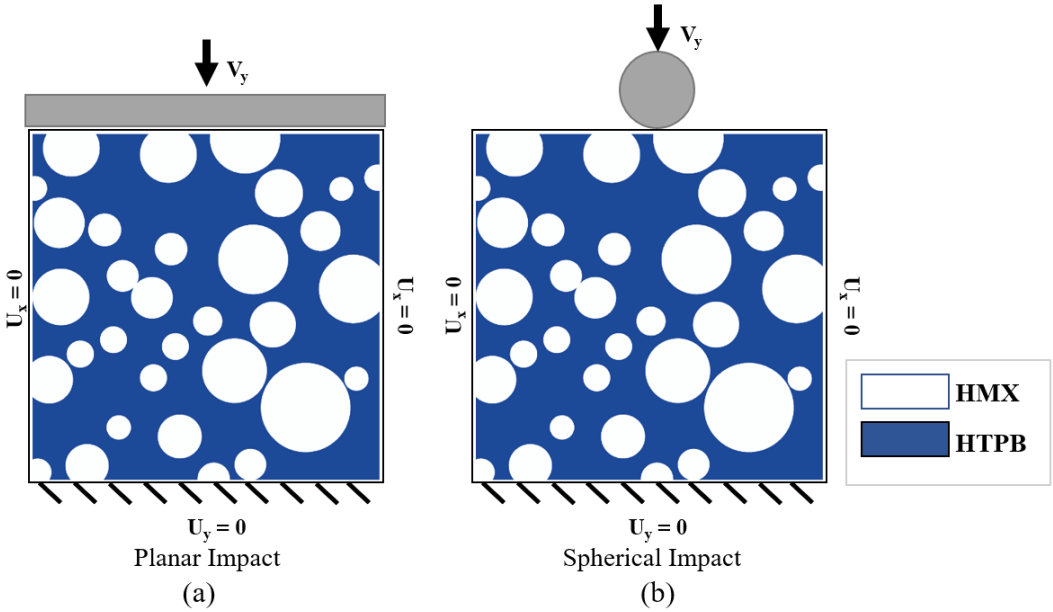

Figure 16: Boundary conditions a) Planar impact b) Spherical impact

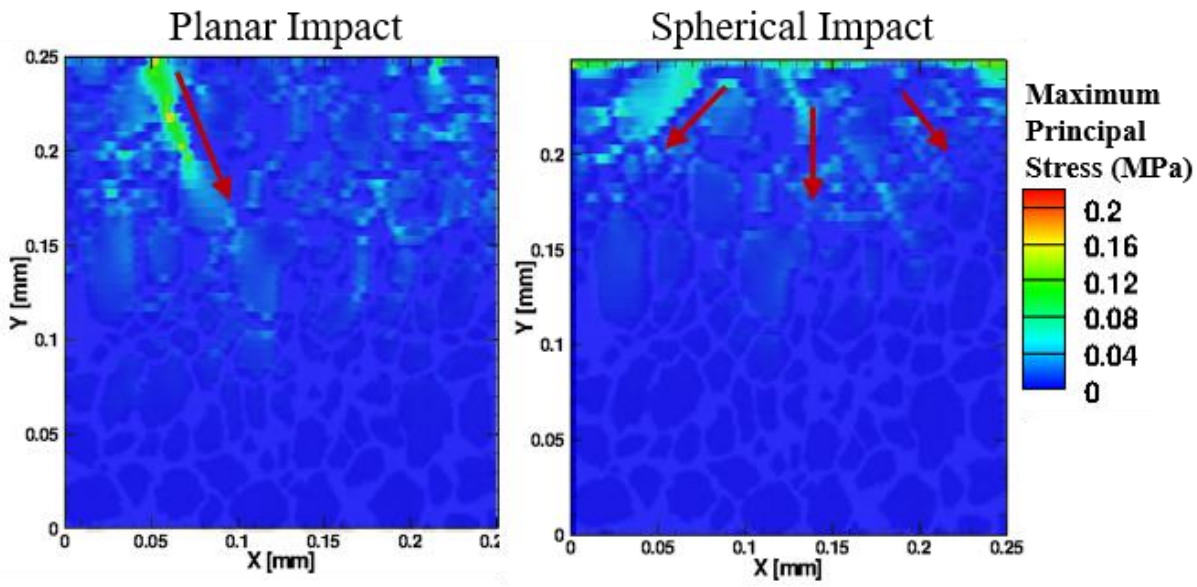

Figure 17: Activation of different force chains in planar vs spherical impact at t=60ns

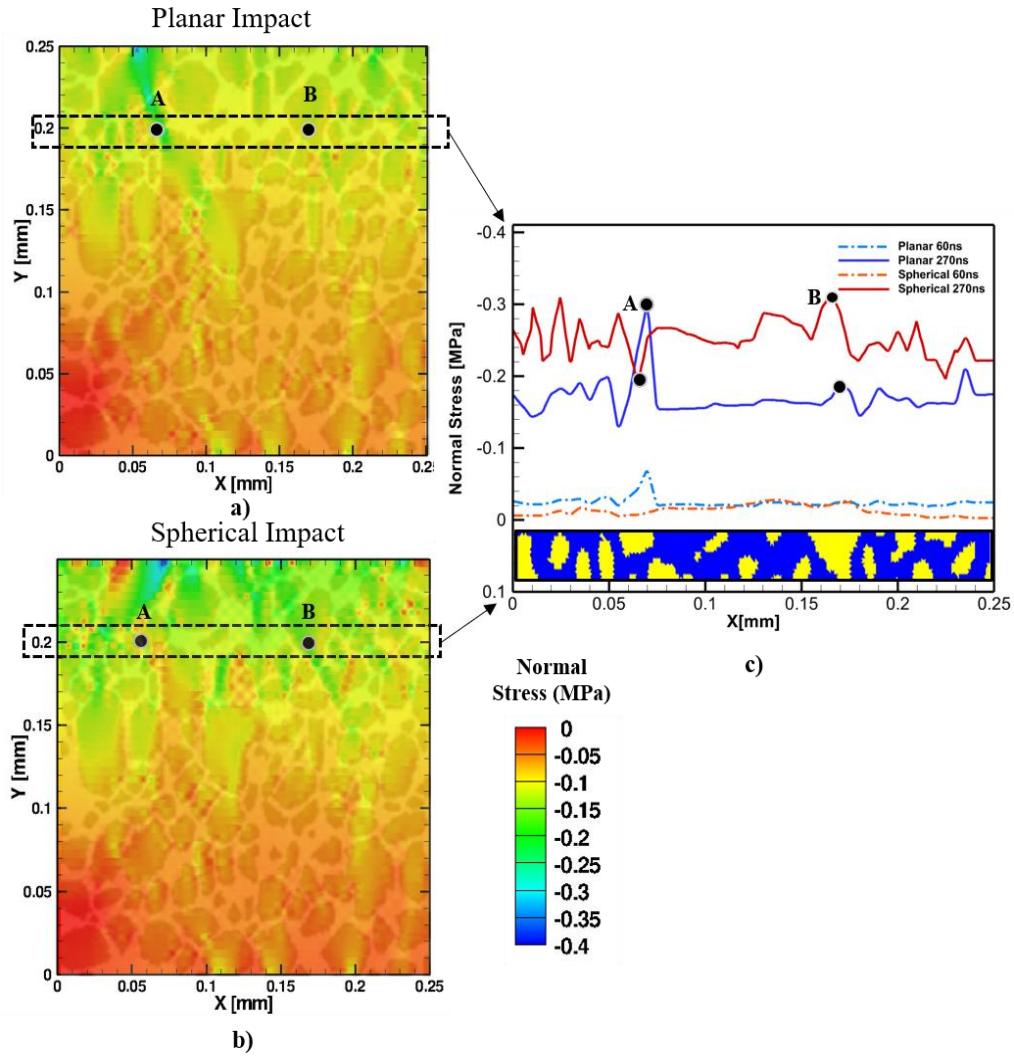

Figure 18: Normal Stress Profile along selected cross section at two different time steps at 0.1m/s at t=270ns

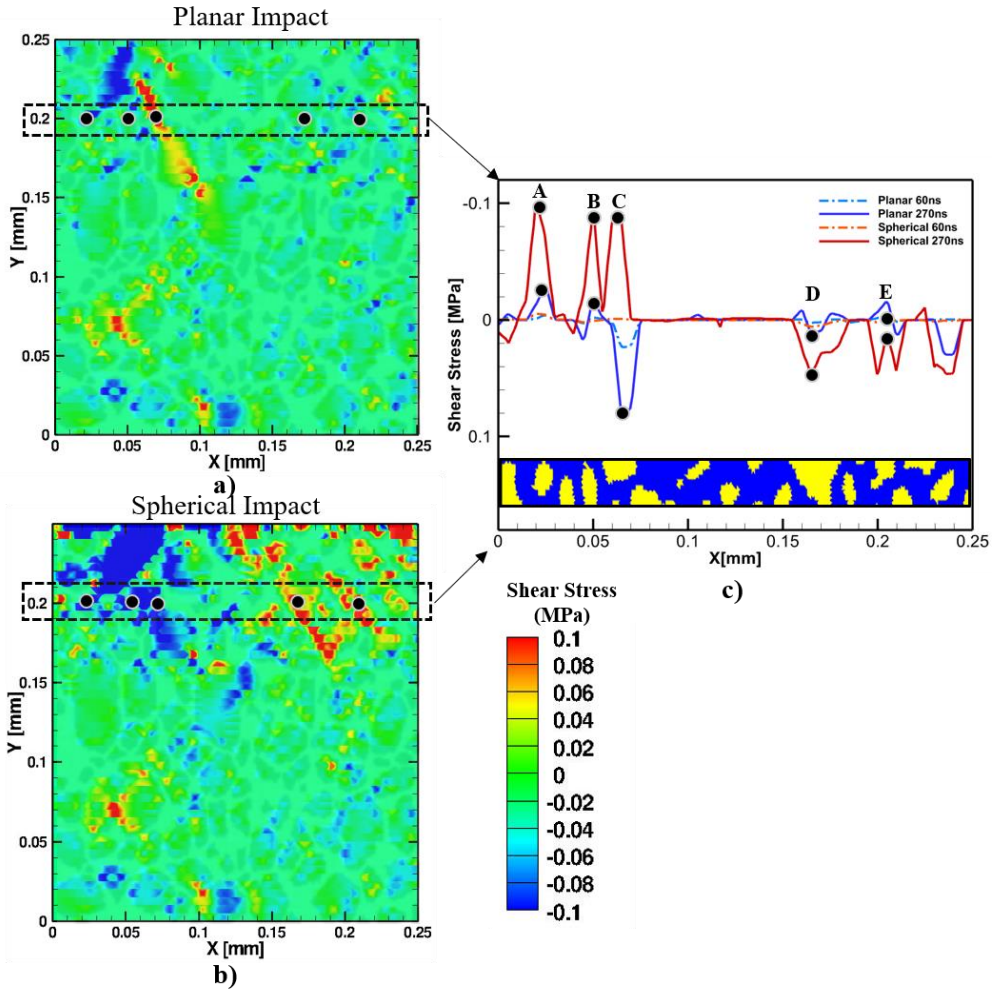

Figure 19: Shear stress profile along selected cross section at two different time steps at 0.1m/s at t= 270ns

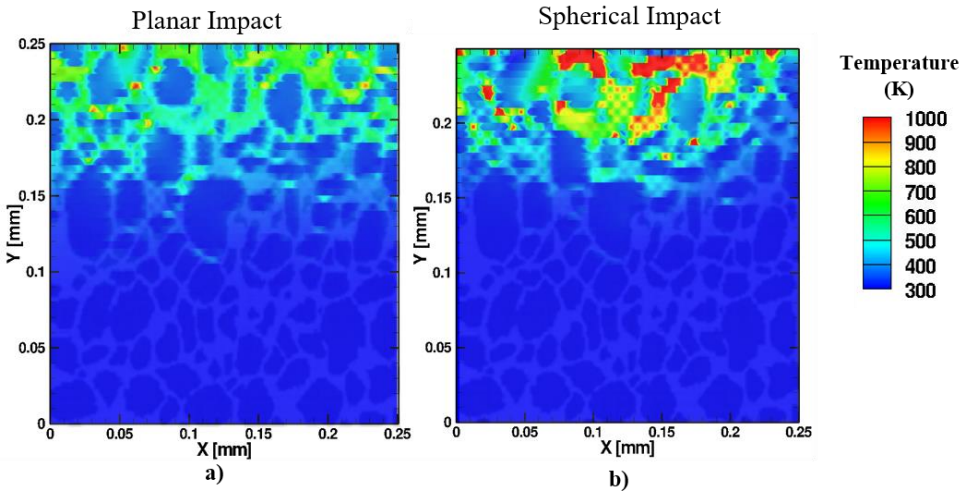

Figure 20: PBX Temperature distribution profile at t= 60 ns

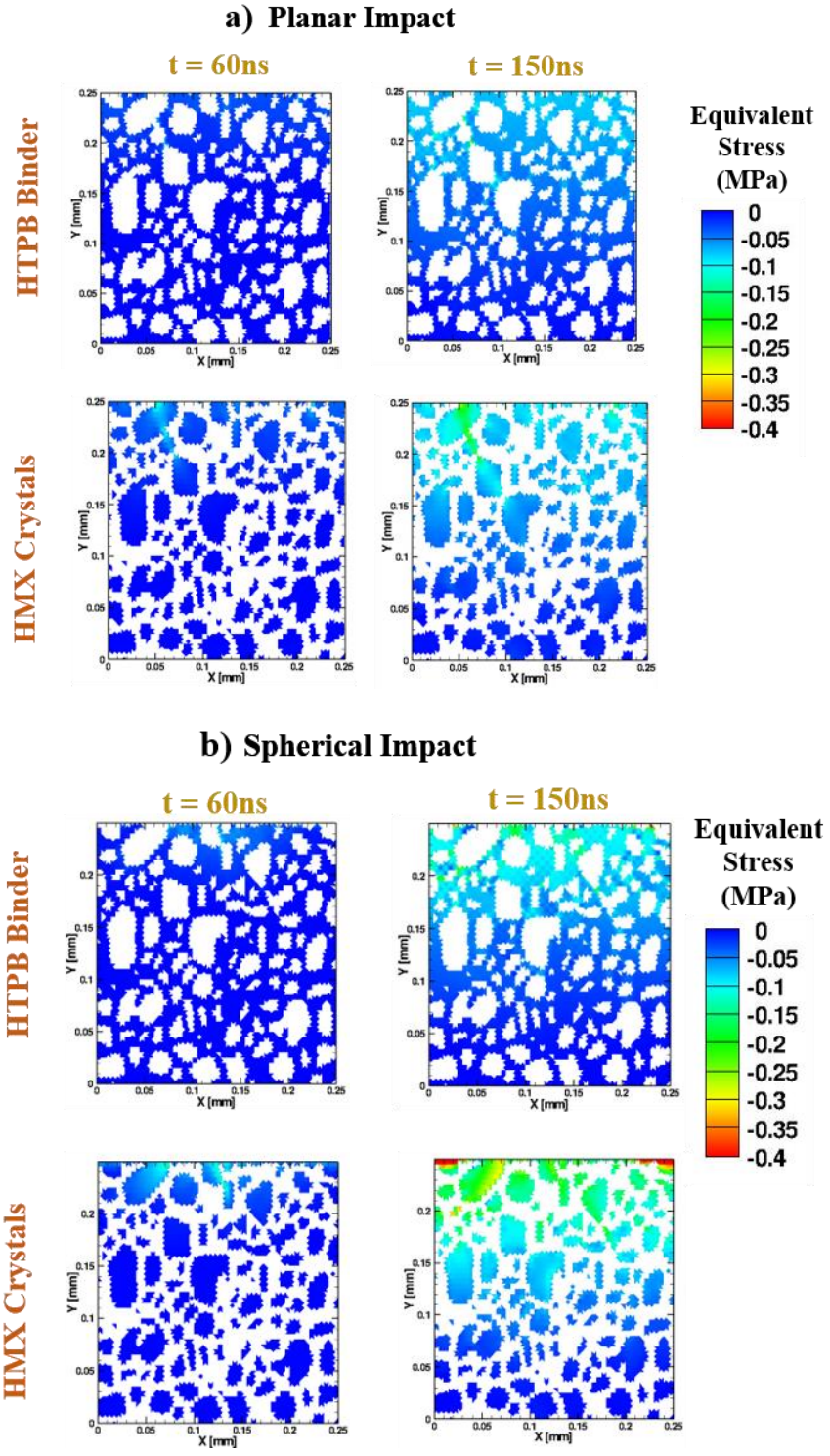

Figure 21: Equivalent Stress distribution with time in crystals and binder in PBX microstructure

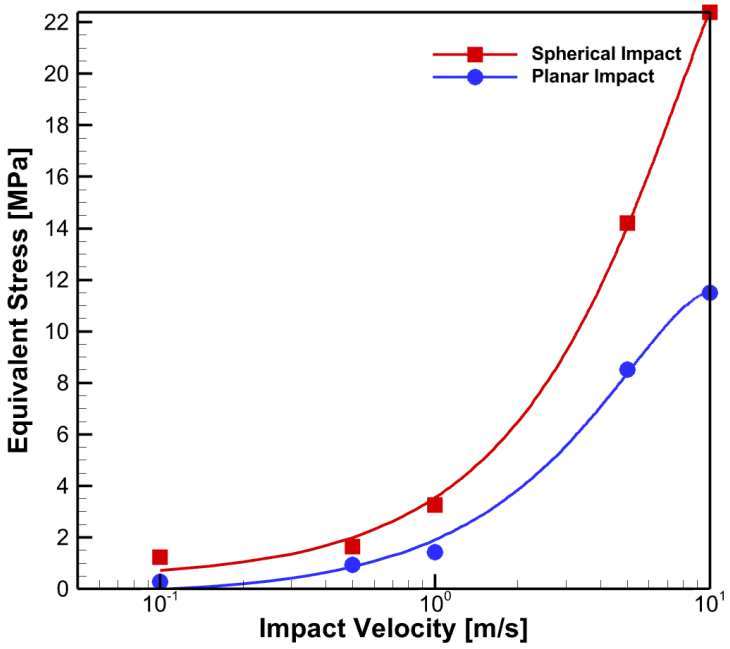

Figure 22: Equivalent Stress with impact velocity

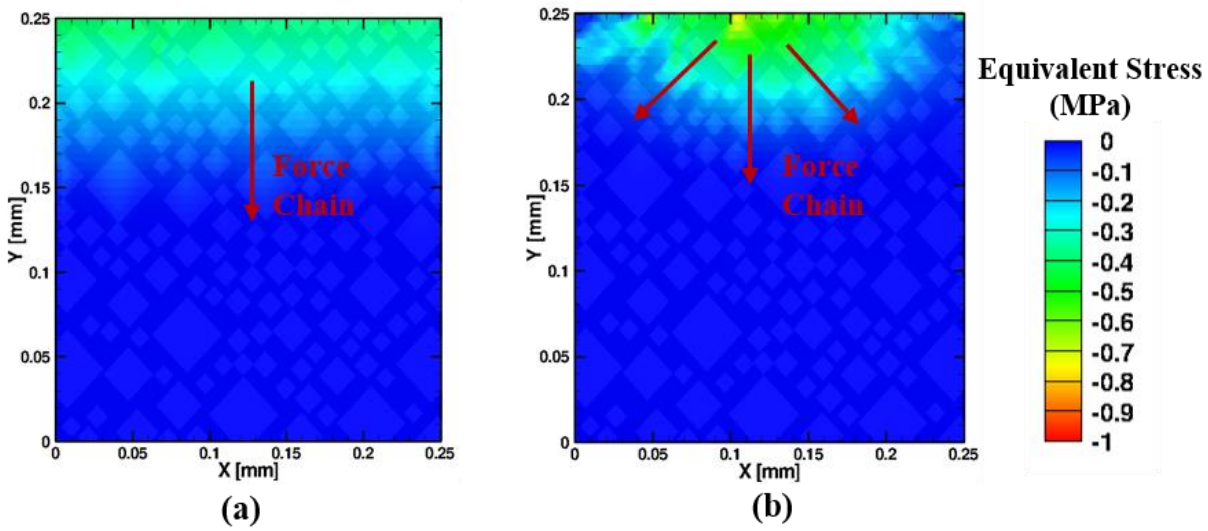

Figure 23: Evolution of stresses in two different impacts in 80% volume fraction of rectangular microstructure

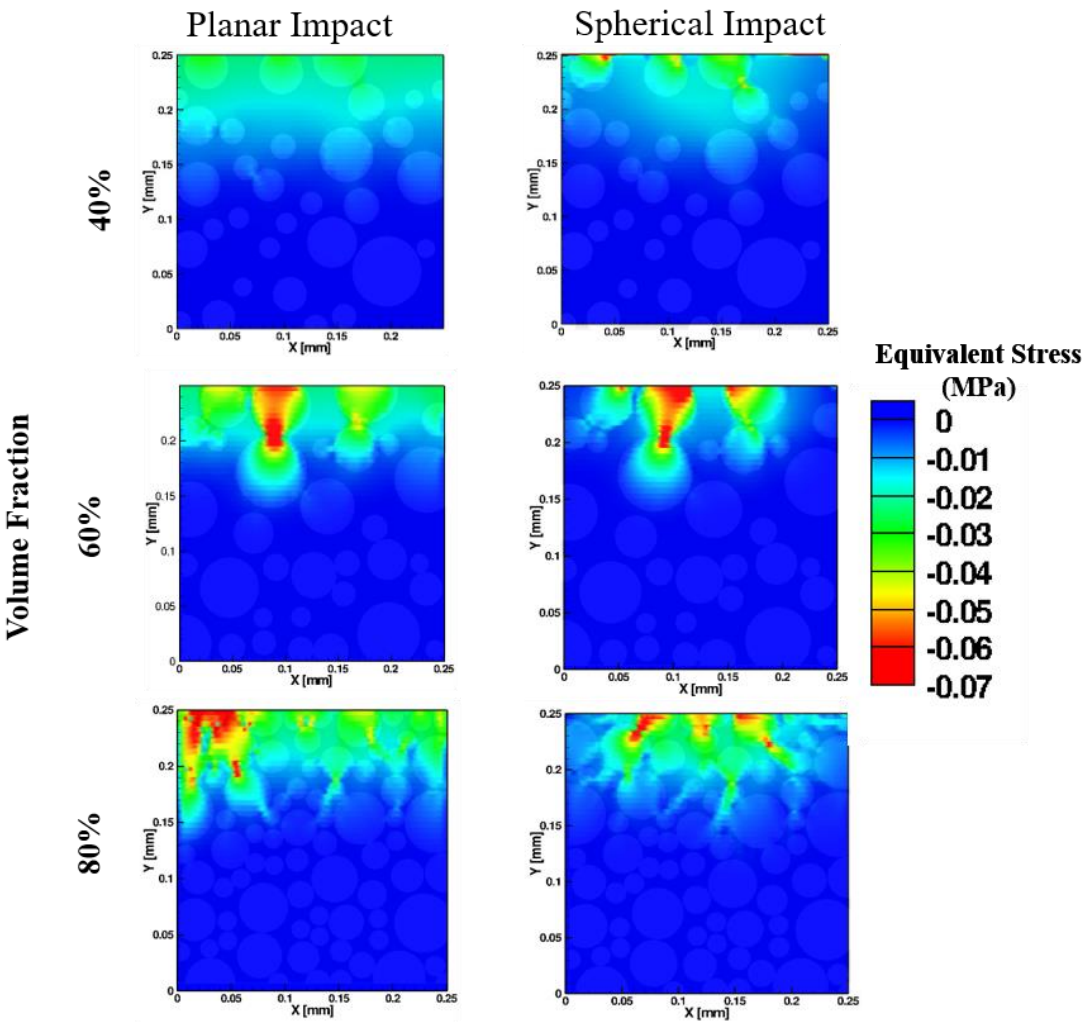

Figure 24: Equivalent Stress in Circular crystal microstructure with varying volume fraction at t=60ns

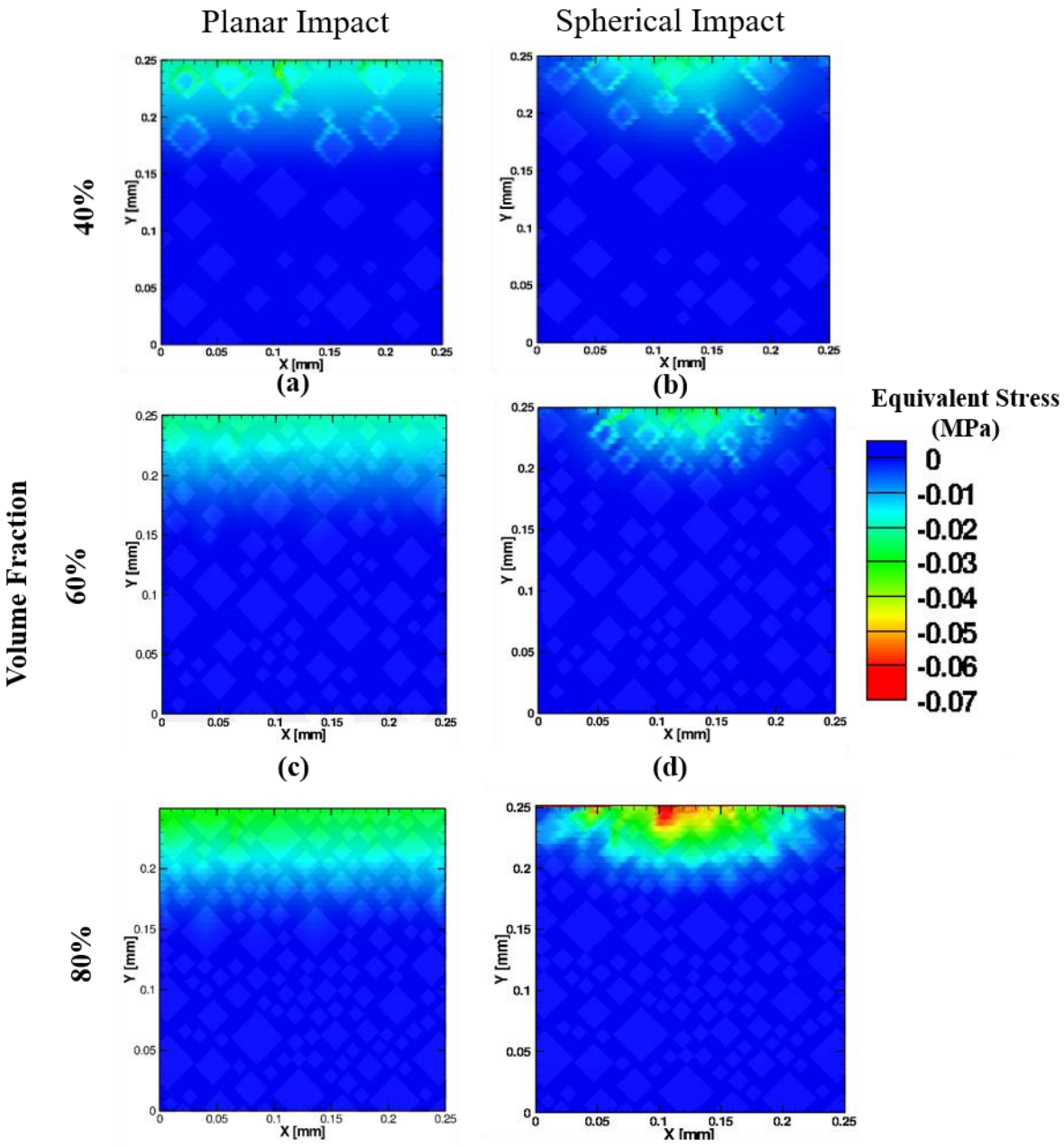

Figure 25: Equivalent Stress in rectangular particle microstructure with varying volume fraction at t=60ns

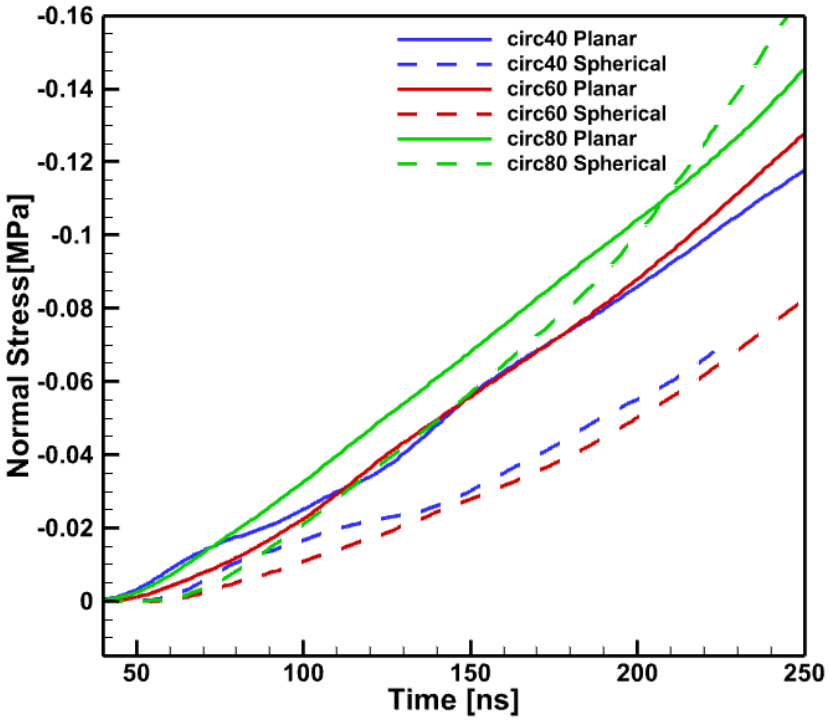

Figure 26: Normal Stress with time in circular crystal microstructure with varying volume fractions

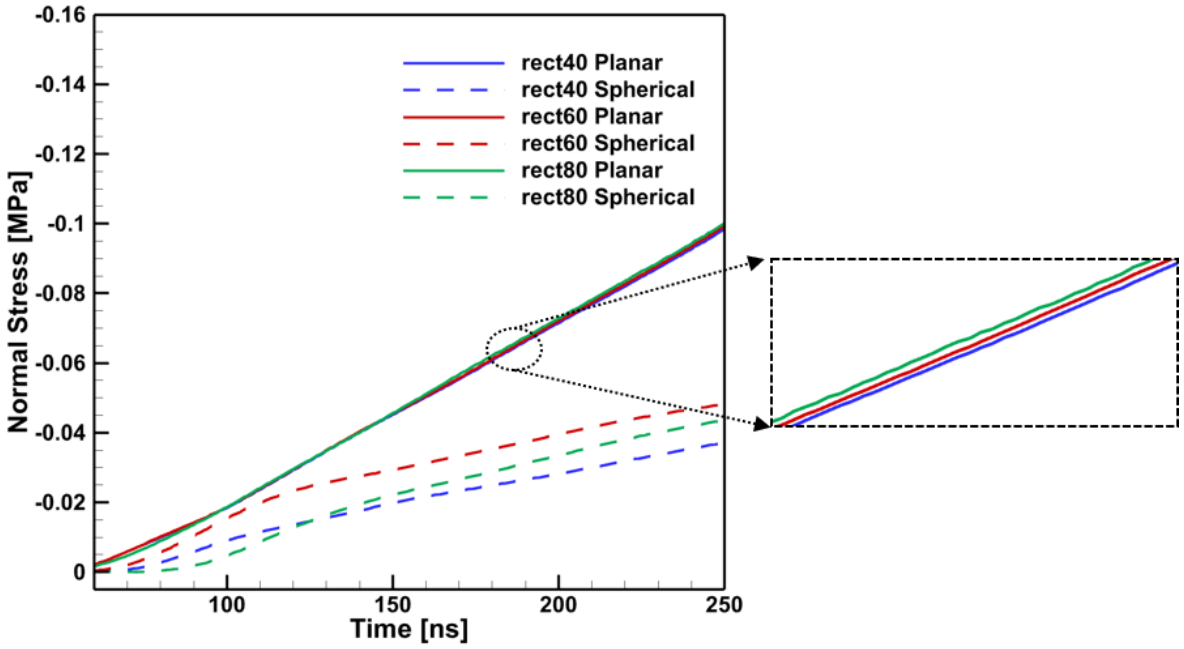

Figure 27: Normal Stress with time in circular crystal microstructure with varying volume fractions

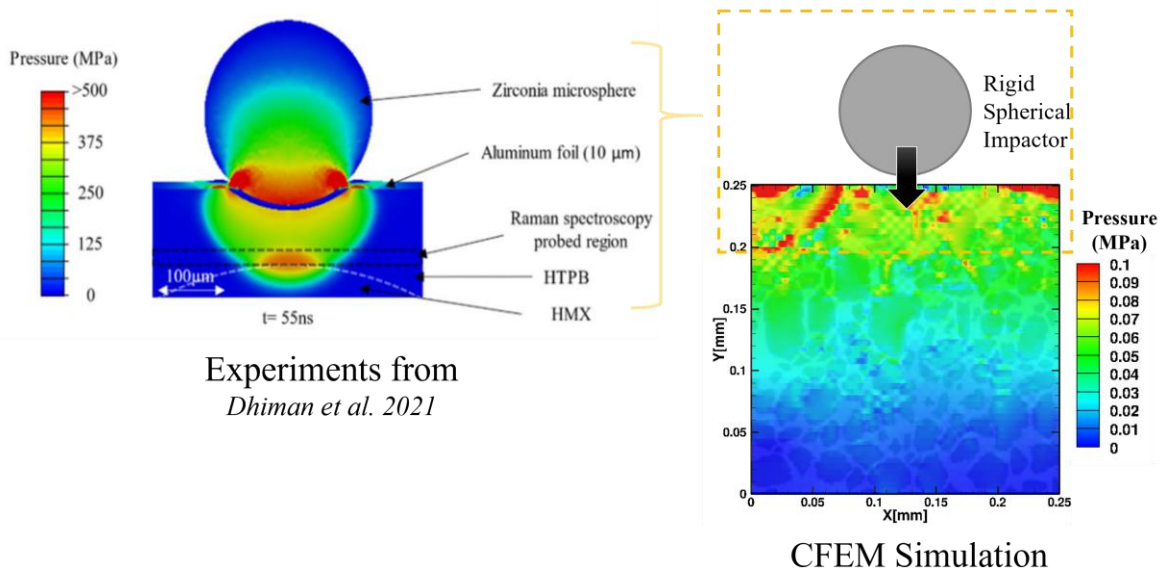

Figure 28: Shock Pressure distribution comparison of experimental and simulation values

3. CONCLUSION

The main objective of this work was to compare spherical and SIs in a computational framework to study the likeliness of hotspot formation under impact in HMX-HTPB material. Two different microstructures were used in this study to highlight the effect of crystal morphology and impact velocities. Cohesive finite element method was used to simulate impact induced failure to obtain stress and temperature profiles.

Some key findings from the present study include - High dependency on microstructure was observed when comparing planar and SIs. Force propagation in microstructures is defined by force chains formed after impact based on crystal morphology. Force chains pointing radially outward was observed in SI whereas force chains pointing downwards was observed in SI. Higher likelihood of hotpot formation was found in SI in the region right below the impact due to the concentration of force in small regions. With increasing impact velocity, the rise in stresses was more significant in spherical impact in comparison to planar impact leading to increased probability of hotspots. With increase in the volume fraction in both circular and rectangular idealized microstructure led to higher normal stresses but propagation of stress wave into the microstructure was higher in planar impact. Larger grain size aided the formation of force chains in spherical impact more than planar impact.

4. FUTURE WORK

The behavior of spherical and planar shapes of impactors on energetic materials was studied. In the present work, the focus was on the initial stages of impact in a planar as well as a SI. An impactor radius of about $1/5^{th}$ of the sample was chosen. The behavior of impact failure might vary based on the maximum particle size in the sample. A parametric study varying particle size with low impact to high impact velocities might be helpful to determine modes of failure from deflagration to detonation. With other particles embedded in a sample, based on the shape of the crystal, it would be interesting to observe the interactions between various sized and shaped particles. For a more realistic model of temperature prediction, cohesive surfaces in three dimensions needs to be modelled to study particles of different shapes. With a longer simulation time and constant impact velocities, tracking the stress waves in spherical impact with a possible reflection at the boundaries of the structure might induce higher stresses which could be worked on in the future.

REFERENCES

[1] J.E. Field, N.K. Bourne, S.J.P. Palmer, and S.M. Walley, "Hot-spot ignition mechanisms for explosives and propellants," *Philosophical Transactions of the Royal Society of London. Series A: Physical and Engineering Sciences*, vol. 339, no. 1654, May 1992, doi: 10.1098/rsta.1992.0034.

[2] A. Barua and M. Zhou, "A Lagrangian framework for analyzing microstructural level response of polymer-bonded explosives," *Modelling and Simulation in Materials Science and Engineering*, vol. 19, no. 5, Jul. 2011, doi: 10.1088/0965-0393/19/5/055001.

[3] D. J. Benson and P. Conley, "Eulerian finite-element simulations of experimentally acquired HMX microstructures," *Modelling and Simulation in Materials Science and Engineering*, vol. 7, no. 3, May 1999, doi: 10.1088/0965-0393/7/3/304.

[4] F. P. Bowden, A. D. Yoffe, and G. E. Hudson, "Initiation and Growth of Explosion in Liquids and Solids," *American Journal of Physics*, vol. 20, no. 4, Apr. 1952, doi: https://doi.org/10.1002/ange.19590712309.

[5] J. G. Bennett, K. S. Haberman, J. N. Johnson, B. W. Asay, and B. F. Henson, "A CONSTITUTIVE MODEL FOR THE NON!SHOCK IGNITION AND MECHANICAL RESPONSE OF HIGH EXPLOSIVES," 1998.

[6] P. J. Rae, H. T. Goldrein, S. J. P. Palmer, J. E. Field, and A. L. Lewis, "Quasi–static studies of the deformation and failure of β –HMX based polymer bonded explosives," *Proceedings of the Royal Society of London. Series A: Mathematical, Physical and Engineering Sciences*, vol. 458, no. 2019, Mar. 2002, doi: 10.1098/rspa.2001.0894.

[7] C. Prakash, A. Olokun, I. Emre Gunduz, and V. Tomar, "Interface Mechanical Properties in Energetic Materials Using Nanoscale Impact Experiment and Nanomechanical Raman Spectroscopy," 2019. doi: 10.1007/978-981-13-3269-2_13.

[8] C. Prakash, I. E. Gunduz, C. Oskay, and V. Tomar, "Effect of interface chemistry and strain rate on particle-matrix delamination in an energetic material," *Engineering Fracture Mechanics*, vol. 191, Mar. 2018, doi: 10.1016/j.engfracmech.2018.01.010.

[9] D. R. Drodge *et al.*, "THE EFFECTS OF PARTICLE SIZE AND SEPARATION ON PBX DEFORMATION," 2009. doi: 10.1063/1.3295067.

[10] C. M. Tarver, S. K. Chidester, and A. L. Nichols, “Critical Conditions for Impact- and Shock-Induced Hot Spots in Solid Explosives †,” *The Journal of Physical Chemistry*, vol. 100, no. 14, Jan. 1996, doi: 10.1021/jp953123s.

[11] R. R. Bernecker and D. Price, “Studies in the transition from deflagration to detonation in granular explosives—I. Experimental arrangement and behavior of explosives which fail to exhibit detonation,” *Combustion and Flame*, vol. 22, no. 1, Feb. 1974, doi: 10.1016/0010-2180(74)90016-9.

[12] G. R. Parker, E. M. Heatwole, M. D. Holmes, B. W. Asay, P. M. Dickson, and J. M. McAfee, “Deflagration-to-detonation transition in hot HMX and HMX-based polymer-bonded explosives,” *Combustion and Flame*, vol. 215, May 2020, doi: 10.1016/j.combustflame.2020.01.040.

[13] K. Yang, Y. Wu, F. Huang, and M. Li, “Numerical simulations of mechanical and ignition-deflagration responses for PBXs under low-to-medium-level velocity impact loading,” *Journal of Hazardous Materials*, vol. 337, Sep. 2017, doi: 10.1016/j.jhazmat.2017.05.008.

[14] J. Zhai, V. Tomar, and M. Zhou, “Micromechanical simulation of dynamic fracture using the cohesive finite element method,” *Journal of Engineering Materials and Technology, Transactions of the ASME*, vol. 126, no. 2, pp. 179–191, Apr. 2004, doi: 10.1115/1.1647127.

[15] A. M. Olokun, C. Prakash, I. Emre Gunduz, and V. Tomar, “The role of microstructure in the impact induced temperature rise in hydroxyl terminated polybutadiene (HTPB)–cyclotetramethylene-tetranitramine (HMX) energetic materials using the cohesive finite element method,” *Journal of Applied Physics*, vol. 128, no. 6, Aug. 2020, doi: 10.1063/5.0011264.

[16] C. Prakash, I. E. Gunduz, and V. Tomar, “Simulation guided experimental interface shock viscosity measurement in an energetic material,” *Modelling and Simulation in Materials Science and Engineering*, vol. 27, no. 8, Dec. 2019, doi: 10.1088/1361-651X/ab4148.

[17] C. Prakash, I. Emre Gunduz, and V. Tomar, “Effect of Strain Rate and Interface Chemistry on Failure in Energetic Materials,” 2018. doi: 10.1007/978-3-319-62831-8_2.

[18] J. Zhai and M. Zhou, “Finite element analysis of micromechanical failure modes in a heterogeneous ceramic material system,” *International Journal of Fracture*, vol. 101, no. 1/2, 2000, doi: 10.1023/A:1007545105723.

[19] A. Barua, Y. Horie, and M. Zhou, “Microstructural level response of HMX–Estane polymer-bonded explosive under effects of transient stress waves,” *Proceedings of the Royal Society A: Mathematical, Physical and Engineering Sciences*, vol. 468, no. 2147, Nov. 2012, doi: 10.1098/rspa.2012.0279.

[20] V. Tomar, “Insights into the effects of tensile and compressive loadings on microstructure dependent fracture of trabecular bone,” *Engineering Fracture Mechanics*, vol. 76, no. 7, May 2009, doi: 10.1016/j.engfracmech.2008.12.013.

[21] D. L. Henann and L. Anand, “A large deformation theory for rate-dependent elastic–plastic materials with combined isotropic and kinematic hardening,” *International Journal of Plasticity*, vol. 25, no. 10, Oct. 2009, doi: 10.1016/j.ijplas.2008.11.008.

[22] M. E. Gurtin and L. Anand, “The decomposition F=FeFp, material symmetry, and plastic irrotationality for solids that are isotropic-viscoplastic or amorphous,” *International Journal of Plasticity*, vol. 21, no. 9, Sep. 2005, doi: 10.1016/j.ijplas.2004.11.007.

[23] G. G. Weber, A. M. Lush, A. Zavaliangos, and L. Anand, “An objective time-integration procedure for isotropic rate-independent and rate-dependent elastic-plastic constitutive equations,” *International Journal of Plasticity*, vol. 6, no. 6, Jan. 1990, doi: 10.1016/0749-6419(90)90040-L.

[24] J. E. Reaugh and E. L. Lee, “Shock hugoniot behavior of mixed phases with widely varying shock imepdances,” 1997.

[25] A. Pi, F. Huang, Y. Wu, and Z. Zhang, “Anisotropic constitutive model and numerical simulations for crystalline energetic material under shock loading,” *Mathematics and Mechanics of Solids*, vol. 19, no. 6, Aug. 2014, doi: 10.1177/1081286513482322.

[26] Y. F. Dafalias, “Issues on the constitutive formulation at large elastoplastic deformations, part 1: Kinematics,” *Acta Mechanica*, vol. 69, no. 1–4, Dec. 1987, doi: 10.1007/BF01175717.

[27] M. C. Boyce, G. G. Weber, and D. M. Parks, “On the kinematics of finite strain plasticity,” *Journal of the Mechanics and Physics of Solids*, vol. 37, no. 5, Jan. 1989, doi: 10.1016/0022-5096(89)90033-1.

[28] V. Tomar, J. Zhai, and M. Zhou, “Bounds for element size in a variable stiffness cohesive finite element model,” *International Journal for Numerical Methods in Engineering*, vol. 61, no. 11, pp. 1894–1920, Nov. 2004, doi: 10.1002/nme.1138.

[29] H. Djojodihardjo and A. S. Mahmud, “Computational Modeling, Simulation, and Tailoring of Nonpenetrating Impact on a Generic Structure,” *Journal of Aerospace Engineering*, vol. 29, no. 3, May 2016, doi: 10.1061/(ASCE)AS.1943-5525.0000531.

[30] C. P. Burger and W. F. Riley, “Effects of impedance mismatch on the strength of waves in layered solids,” *Experimental Mechanics*, vol. 14, no. 4, Apr. 1974, doi: 10.1007/BF02322835.

[31] J. L. Davis, *Wave Propagation in Solids and Fluids*. New York, NY: Springer New York, 1988. doi: 10.1007/978-1-4612-3886-7.

[32] A. Dhiman, A. Olokun, and V. Tomar, “Microscale Analysis of Stress Wave Propagation Through Plastic Bonded Explosives Under Micro-Sphere Shock Impact,” *Journal of Dynamic Behavior of Materials*, vol. 7, no. 2, Jun. 2021, doi: 10.1007/s40870-021-00290-y.

[33] S. Kim, A. Barua, Y. Horie, and M. Zhou, “Ignition probability of polymer-bonded explosives accounting for multiple sources of material stochasticity,” *Journal of Applied Physics*, vol. 115, no. 17, May 2014, doi: 10.1063/1.4874915.

[34] Virginia Manner, Marc J Cawkwell, Geoff W Brown, and John D Yeager, “Examining the Effects of Crystal Structure and Bonding on Explosive Impact Sensitivity,” 2019.

[35] A. M. Olokun, C. Prakash, I. Emre Gunduz, and V. Tomar, “The role of microstructure in the impact induced temperature rise in hydroxyl terminated polybutadiene (HTPB)–cyclotetramethylene-tetranitramine (HMX) energetic materials using the cohesive finite element method,” *Journal of Applied Physics*, vol. 128, no. 6, Aug. 2020, doi: 10.1063/5.0011264.

[36] F. Radjai, D. E. Wolf, M. Jean, and J.-J. Moreau, “Bimodal Character of Stress Transmission in Granular Packings,” *Physical Review Letters*, vol. 80, no. 1, Jan. 1998, doi: 10.1103/PhysRevLett.80.61.

[37] A. Needleman and M. Ortiz, “Effect of boundaries and interfaces on shear-band localization,” *International Journal of Solids and Structures*, vol. 28, no. 7, 1991, doi: 10.1016/0020-7683(91)90005-Z.